https://doi.org/10.5194/wes-2020-104
Preprint. Discussion started: 24 September 2020

eawe european academy of wind energy
Open Access WIND ENERGY SCIENCE DISCUSSIONS

Wind turbine load validation in wakes using field reconstruction techniques and nacelle lidar wind retrievals

Davide Conti[1], Vasilis Pettas[2], Nikolay Dimitrov[1], and Alfredo Peña[1]

[1]Department of Wind Energy, Technical University of Denmark, Frederiksborgvej 399, 4000 Roskilde, Denmark
[2]Stuttgart Wind Energy (SWE), University of Stuttgart, Allmandring 5b, 70569 Stuttgart, Germany

Correspondence: Davide Conti (davcon@dtu.dk)

Abstract. This study proposes two methodologies for improving the accuracy of wind turbine load assessment under wake conditions by combining nacelle-mounted lidar measurements with wake wind field reconstruction techniques. The first approach consists in incorporating wind measurements of the wake flow field, obtained from nacelle lidars, into random, homogeneous Gaussian turbulence fields generated using the Mann spectral tensor model. The second approach imposes wake deficit time-series, which are derived by fitting a bivariate Gaussian shape function on lidar observations of the wake field, on the Mann turbulence fields. The two approaches are numerically evaluated using a virtual lidar simulator, which scans the wake flow fields generated with the Dynamic Wake Meandering (DWM) model. The lidar-reconstructed wake fields are input to aeroelastic simulations of the DTU 10 MW wind turbine and the resulting load predictions are compared with loads obtained with the $target$ (no lidar-based) DWM simulated fields. The accuracy of load predictions is estimated across a variety of lidar beam configurations, probe volume sizes, and atmospheric turbulence conditions. The results indicate that the 10-min power and fatigue load statistics, predicted with lidar-reconstructed fields, are comparable with results obtained with the DWM simulations. Furthermore, the simulated power and load time-series exhibit a high level of correlation with the $target$ observations, thus decreasing the statistical uncertainty (realization-to-realization) by a factor between 1.2 and 5, compared to results obtained with the $baseline$, which is DWM simulated fields with different random seeds. Finally, we show that the spatial resolutions of the lidar's scanning strategies as well as the size of the probe volume are critical aspects for the accuracy of the reconstructed wake fields and load predictions.

1 Introduction

Wind turbines operating under wake conditions experience higher loading conditions and lower power productions compared to those operating under wake-free conditions (Barthelmie et al., 2009; Larsen et al., 2013). The wake-induced velocity deficit and its spatial displacement, also referred to as wake meandering, are critical aspects in both loads and power analyses (Madsen et al., 2010; Doubrawa et al., 2017). The former reduces the inflow wind speed and causes unbalanced aerodynamic load

https://doi.org/10.5194/wes-2020-104
Preprint. Discussion started: 24 September 2020

distribution at the rotor, which in turn induces high load cycle amplitudes in the whole wind turbine structure (Lee et al., 2012), whereas the latter is the main source of wake added turbulence (Madsen et al., 2010), affecting wind turbine responses and inducing high fatigue damage (Larsen et al., 2013). Moreover, small turbulence eddies that result from the breakdown of the tip vortices can cause small fatigue load cycles (Madsen et al., 2005). Thus, aeroelastic analysis of wind turbines operating under wake condition requires a detailed modeling of the wake flow fields.

For the purpose of load validation, the IEC 61400-1 standard (IEC, 2019) recommends engineering wake models, which ensures low computational effort and an acceptable level of accuracy. The DWM model is a low fidelity physical model, recommended by the IEC standard, which simulates wind field time series including wake deficits together with a stochastic meandering model. The motions of the wake deficits are super-imposed on random three-dimensional turbulence fields serving as input for aeroelastic simulations. The wake characteristics simulated by the DWM model are conditional both on the ambient conditions, which can be measured from a local meteorological mast, and the operational conditions of the upstream wind turbines. In order to carry out load simulations, the 10-min statistical properties (mean and variance) of the simulated ambient and operational conditions are set to match the measured ambient wind statistics (Dimitrov and Natarajan, 2017). However, since the synthetic turbulence realization, as well as the wake meandering, are stochastic processes, the instantaneous velocities of the simulated wake wind field and the resulting load prediction time-series are not synchronized with the true observations. This can lead to simulation errors (Zwick and Muskulus, 2015) and introduces high statistical uncertainty on load predictions (Dimitrov and Natarajan, 2017; Pedersen et al., 2019). Further, statistics from a large set of simulations are required to compensate for the large load variations.

Alternative load verification procedures are being explored to potentially reduce the statistical and modelling uncertainty of engineering wake models, as well as to replace measurements from masts with those from Doppler lidars (Dimitrov et al., 2019; Reinwardt et al., 2020; Conti et al., 2020). Lidars can provide high spatial and temporal resolution inflow observations and extend (and eventually replace) traditional point-like measurements such as those from cup and sonic anemometers. In particular, nacelle-mounted lidars have the advantage to be aligned with the rotor, which increases the amount of validation data. The feasibility of nacelle-mounted lidar observations has been demonstrated for wake characterization (Trujillo et al., 2011; Fuertes et al., 2018; Herges and Keyantuo, 2019; Reinwardt et al., 2020), lidar-assisted control (Schlipf et al., 2013; Simley et al., 2013, 2018), and power and load analysis in freeestream conditions (Wagner et al., 2014; Dimitrov et al., 2019). The recent work of Conti et al. (2020) demonstrated that lidar-based load validation procedure in wakes should account for a model of the wake deficit and its dynamics.

The present work proposes two alternative approaches for wind turbine load validation under wake conditions using nacelle-mounted lidar measurements combined with wake field reconstruction techniques. The first approach builds on the work of Dimitrov and Natarajan (2017), which incorporates multiple lidar retrievals in a turbulence field generated using the Mann spectral model (Mann, 1994) through a constrained Gaussian field algorithm. The second approach reconstructs wake deficit characteristics and their motions by fitting a bivariate Gaussian shape function on lidar retrievals and superimposes these deficits on a random realization of the Mann turbulence field. We evaluate these methods on a numerical study that simulates a nacelle-mounted lidar scanning the synthetic wake flow fields generated with the DWM model. Thus, we carry out aeroelastic

https://doi.org/10.5194/wes-2020-104
Preprint. Discussion started: 24 September 2020

simulations of the DTU 10 MW wind turbine (Bak et al., 2013) with the lidar-reconstructed fields, and evaluate the accuracy of load predictions against results obtained with the $target$ non lidar-based DWM simulated fields. In this study, we make use of two sets of independent turbulence seed realizations to quantify the statistical uncertainty of load predictions inherent of the DWM model. The main objective of this study is to verify that, when compared to the $target$ loads, the load prediction obtained using lidar-reconstructed wake flow fields is as accurate or superior than that obtained with the DWM model using turbulence parameters matching the measured ambient wind statistics, which is the standard $baseline$.

The work is structured as follows. In Sect. 2, we briefly formulate the load validation procedure. Section 3 introduces the methodology including the Mann spectral tensor model (Sect. 3.1) and the DWM model (Sect. 3.2). Section 3.3 describes the virtual lidar simulator and the analyzed scanning configurations. The wake field reconstruction techniques are formulated in Sect. 3.4. The results are provided in Sect. 4, including the uncertainty analysis of the lidar-reconstructed fields in relation to the target wake fields in Sect. 4.1, a detailed analysis of the load validation results in Sect. 4.2, and the sensitivities of the lidar specifications, e.g., probe volume size and sampling frequency, and those related to the atmospheric inflow conditions on the load predictions accuracy in Sect. 4.3. The last two sections are dedicated to the discussion of the findings and the conclusions from the study.

2 Problem formulation

The design load cases (DLCs) and load verification procedure for wind turbines operating in wakes are described in the IEC standards (IEC, 2015, 2017, 2019). The present work covers the analysis of fatigue loads of wind turbines operating in wakes (see IEC 61400-1, DLC1.2). Following the approach of Dimitrov and Natarajan (2017), we use two sets of random turbulence realizations (also referred to as seeds), which we denote as *set A* and *set B*. We simulate DWM-based wake fields using turbulence seeds from *set A*, which we denote as the *target* fields. We also generate a second set of DWM-based wake fields using seeds from *set B*, which we denote as *baseline*. Since *set A* and *set B* come from the same distributions but are statistically independent, we expect that the outcomes of load simulations with *set A* and *set B* will have the same statistical properties, but will not be correlated. Hence, the result of a one-to-one comparison of load statistics between the realizations in the *baseline* and the *target* simulations is a direct measure of the statistical uncertainty (i.e., load scatter) that originates from both the random turbulence realizations and the stochastic meandering process.

To evaluate the lidar-based approaches, we use a virtual lidar simulator that scans the *target* wake fields, and, through a field reconstruction technique, incorporates these samples in a random turbulence seed from *set B*. This numerical approach intends to imitate what we would eventually do when nacelle lidar measurements within wakes are available for load predictions. Further, by incorporating lidar retrievals in the field reconstruction technique, we expect to reduce the amount of statistical uncertainty as the load time series resulting from this approach will have greater similarity with the load time series based on the *target* turbulence fields. Therefore, this procedure allows us to quantify the uncertainty of load predictions that results from lidar-reconstructed wake fields against the *target*, and at the same time, to compare the associated statistical uncertainty with that of the *baseline*. To summarize, the following load simulation cases are defined:

https://doi.org/10.5194/wes-2020-104
Preprint. Discussion started: 24 September 2020

- *Target*: DWM-based wake fields imposed on random turbulence seeds from *set A*.
- *Baseline*: DWM-based wake fields imposed on random turbulence seeds from *set B*.
- *Constrained simulations (CS)*: lidar-reconstructed wake fields, where lidar virtual measurements of the *target* fields are incorporated as constraints to random turbulence field realizations from *set B*.
- *Wake deficit simulations (WDS)*: lidar-reconstructed wake fields, where lidar virtual measurements of the *target* fields are fitted to a wake deficit shape function to compute wake deficits, which are then superimposed to random turbulence field realizations from *set B*.

The load validation comprises a large number of simulations in order to quantify the statistical uncertainty of load predictions under a variety of inflow conditions. Eventually, we quantify the load uncertainties of the *baseline*, *CS* and *WDS* by comparison to the loads of the *target* simulations, and we define two main criteria to evaluate the proposed approaches:

I The mean bias of load predictions obtained with the lidar-reconstructed *CS*- and *WDS*-simulations is of the same order of that obtained with the *baseline*.

II The statistical uncertainty (i.e. standard deviation of the bias) derived with the lidar-reconstructed *CS*- and *WDS*-simulations is lower than that obtained with the *baseline*.

Provided that these criteria are satisfied, the proposed lidar-based reconstruction approaches will produce (I) load predictions in wakes, which are in a statistical sense as accurate as the DWM model and (II) a reduced statistical uncertainty by reconstructing wake fields that have stronger similarities to the $target$ fields compared to the DWM model results.

3 Methodology

3.1 Mann turbulence spectral model

The time-domain aeroelastic simulations require input of a three-dimensional turbulence field that mimics atmospheric turbulence (Dimitrov et al., 2017). For this purpose, the IEC 61400-1 recommends, i.a., the Mann uniform shear spectral tensor model (Mann, 1994). The turbulence spectral properties of a three-dimensional homogeneous wind field are described by the spectral velocity tensor $\Phi_{ij}(\boldsymbol{k})$ (Kristensen et al., 1989):

$$\Phi_{ij}(\boldsymbol{k}) = \frac{1}{(2\pi)^3}\int R_{ij}(\boldsymbol{r})\exp(i\boldsymbol{k}\cdot\boldsymbol{r})d\boldsymbol{r}, \quad (1)$$

which is the Fourier transform of the covariance tensor $R_{ij}(\boldsymbol{r})$, $\boldsymbol{r} = (x,y,z)$ is the spatial separation vector defined in a right-handed coordinate system such that the longitudinal component of the wind field is in the x direction, y and z are the directions of the transversal components, and $\boldsymbol{k} = (k_1,k_2,k_3)$ is the wave vector with the wavenumbers in the (x,y,z) directions. The model by Mann (1994) (hereafter referred to as the Mann model), assumes neutral atmospheric conditions and defines the

https://doi.org/10.5194/wes-2020-104
Preprint. Discussion started: 24 September 2020

spectral tensor as function of three input parameters: $\alpha_k \epsilon^{2/3}$, which is a product of the spectral Kolmogorov constant α_k and the turbulent energy dissipation rate ϵ, Γ is a parameter describing the anisotropy of the turbulence, and L is a length scale proportional to the size of turbulence eddies. From the spectral tensor, the cross-spectra between two points located in a y–z plane and separated by a distance (Δ_y, Δ_z) are calculated numerically by:

$$\chi_{ij}(\boldsymbol{k}, \Delta_y, \Delta_z) = \int\int \Phi_{ij}(\boldsymbol{k}, \alpha_k \epsilon^{2/3}, L, \Gamma) \exp(ik_2\Delta_y + ik_3\Delta_z) dk_2 dk_3. \tag{2}$$

Further, by inverse Fourier-transforming the cross spectrum χ_{ij}, we can derive the auto- and cross-correlation structure of the turbulence field (Dimitrov and Natarajan, 2017), as

$$R_{ij}(\Delta_x, \Delta_y, \Delta_z) \propto \int \chi_{ij}(k_1, \Delta_y, \Delta_z) \exp(ik_1\Delta_x) dk_1. \tag{3}$$

3.2 Dynamic Wake Meandering model

The DWM model simulates the lateral and vertical movements of the wake deficit by superimposing these deficits on a random and homogeneous turbulent wind field, e.g., that generated using the Mann model. The velocity deficit definition is based on the work of Ainslie (1986, 1988), who applied a thin shear-layer approximation of the Navier–Stokes equations and a simple eddy viscosity formulation. The wake deficit development downstream of the generating turbine is driven by the turbulent mixing occurring due to the ambient turbulence and the turbulence generated by the wake shear field itself (Madsen et al., 2010). The recent work of Keck et al. (2014, 2015) included atmospheric stability effects on the eddy viscosity formulation. The wake-added turbulence that originates from the breakdown of tip vortices and from the shear of the velocity deficit is accounted for by a semi-empirical turbulence scaling factor. This factor scales the residual field of a Mann-based turbulence field generated assuming isotropic turbulence, i.e., $\Gamma = 0$, and a small turbulence length scale ($L \approx 10$–25% of the ambient turbulence length scale) (Madsen et al., 2010). Both the wake deficit and wake-added turbulence profiles are resolved in the meandering frame of reference, which is a coordinate system with origin in the center of symmetry of the wake deficit. The DWM model considers wakes as passive tracers driven by the large turbulence scales of the inflow. Madsen et al. (2010) defined large turbulent scales as those measuring two rotor diameters (D) or larger, an assumption validated using lidar observations of wake fields (Bingöl et al., 2010; Trujillo et al., 2011). The wake is advected downstream with the mean wind speed using Taylor's frozen turbulence hypothesis. Recent studies have calibrated and validated the DWM-predicted wake deficits against high-fidelity wake field simulations (Keck et al., 2014, 2015), wind turbine operational data (Larsen et al., 2013) and only recently, lidar measurements of the wake field (Reinwardt et al., 2020). Figure 1 shows the wake deficit (K_{def}) and wake-added turbulence profiles (K_{mt}) derived from the DWM model and the DTU 10 MW wind turbine, as function of ambient wind speed and turbulence. As illustrated, the depth of the wake deficit decreases for increasing inflow wind speed and turbulence, due to the reduced rotor thrust coefficient and the enhanced turbulence mixing. The wake-added turbulence is proportional to the depth and gradient of the velocity deficit profile; thus a faster recovery of the deficit induces lower added turbulence.

https://doi.org/10.5194/wes-2020-104
Preprint. Discussion started: 24 September 2020

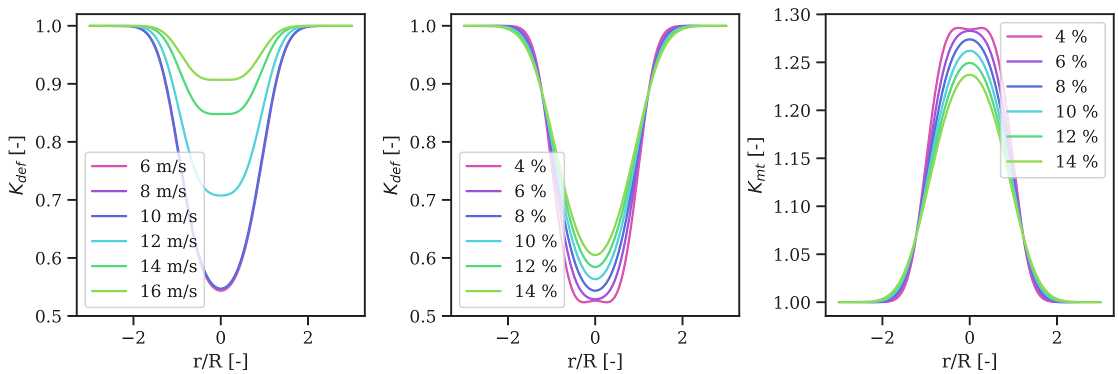

Figure 1. Steady wake characteristics predicted by the DWM model at the downstream distance of 5 D, D being the rotor diameter, resolved in the radial direction and normalized on the rotor radius (R = 89.5 m). Left and middle: wake deficit profiles as function of ambient wind speed and ambient turbulence. Right: wake-added turbulence profiles as function of the ambient turbulence.

3.3 Lidar simulator

We use the lidar simulator developed within the ViConDAR open source numerical framework to virtually replicate lidar measurements (https://github.com/SWE-UniStuttgart/ViConDAR), (Pettas et al., 2020). The lidar simulator derives the line-of-sight (LOS) velocities at each scanning location, by transforming the u-, v- and w-velocity components of the synthetic turbulence field into a LOS coordinate system. To simulate the probe volume of the lidars, a Gaussian weighting function $W(F,r)$ is imposed along the LOS coordinate r and centered at the focal distance F:

$$V_{LOS,eq} = \int V_{LOS}(r)W(F,r)dr. \tag{4}$$

The u-velocity is computed from the projection of $V_{LOS,eq}$ onto the longitudinal axis, i.e., the v- and w-velocity components are neglected in the field reconstruction (Schlipf et al., 2013; Simley et al., 2013; Pettas et al., 2020). The latter increases the uncertainty of the procedure. Other sources of uncertainty inherent to the use of lidars, e.g., optics and internal signal processing, are accounted for by adding a Gaussian white noise. Here we add noise at a level that results in a signal-to-noise ratio of -20 dB, as shown in Pettas et al. (2020). We do not investigate the sensitivity of the noise level in the present work. The lidar simulator can mimic any arbitrary scanning pattern and includes a time-lag between each lidar-sampled measurements to resemble the scanning frequency (see Fig. 2). In the present study, the virtual lidar data are computed from the synthetic wake flow fields generated using the DWM model. These wind fields are time series of the u-, v- and w-velocity components defined over a turbulence box with a grid size of 8192$\times$32$\times$32 (x,y,z). A spatial resolution of 6.5 m is used for the grid in the rotor plane, which leads to a turbulence box with dimension 208 m $\times$ 208 m in both lateral and vertical directions (y,z), while the spatial resolution in the longitudinal axis depends on the simulated wind speed. These dimensions ensure an adequate

https://doi.org/10.5194/wes-2020-104
Preprint. Discussion started: 24 September 2020

turbulence field for a 10 min wind field simulation over a large rotor, and a space-time resolution such that the probe volume effects can be captured by the virtual lidar.

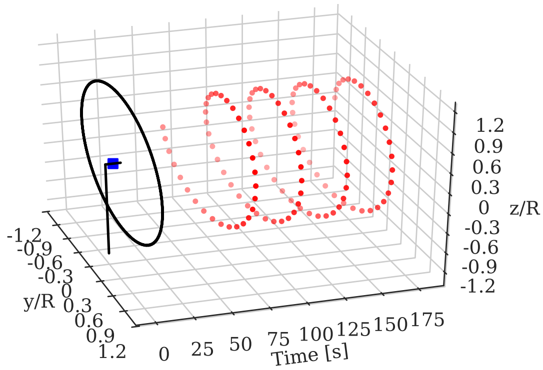

Figure 2. An illustration of the virtual lidar simulator setup run for 175 s. The wind turbine is sketched by the black solid lines, the nacelle-mounted lidar is represented by a blue squared marker measuring upfront the turbine. The trajectory of the scanning beam is shown by discrete red dots.

3.3.1 Lidar scanning strategies

Several nacelle-mounted lidars have been developed both for commercial and research purposes. These include continuous-wake (CW) and pulsed lidar (PL) technologies. The CW and PL lidars differ in the emission waveform, and in the temporal and spatial resolution, among others (Peña et al., 2015). The Windar Photonics 2- and 4-beam CW lidars have been applied for wake detection purposes (Held and Mann, 2019a) and rotor-effective wind speed estimation (Held and Mann, 2019b). The ZephIR Dual Mode (DM) circular-scanning CW lidar, with a single beam and sampling frequency of approximately 50 Hz, has been used for several purposes including power curve assessment (Medley et al., 2014), wind field reconstruction (Borraccino et al., 2017), turbulence characterization (Peña et al., 2017), and load validation in both free and wake conditions (Dimitrov et al., 2019; Conti et al., 2020). Based on the ZephIR, a research lidar, the SpinnerLidar (SL), was developed (Peña et al., 2019). The SL uses two rotating prisms that scan the inflow at 400 points in 1–2 s. Due to the scanning pattern, the SL can be used for detailed wake characterization (Herges and Keyantuo, 2019; Doubrawa et al., 2019). A five-beam PL lidar developed by Avent Lidar Technology was used in several experiments (Bos et al., 2016; Borraccino et al., 2017). This lidar does not longer exist, but a 4-beam version by Leosphere is on the market. The lidar developed by the Stuttgart Wind Energy (SWE) group builds on the commercial Windcube WLS-7 from Leosphere and is adapted with a scanner device with two degrees of freedom for nacelle installation in order to scan the wind field in any direction. Currently, the SWE lidar scans at five ranges with a maximum of 49 points per range in approximately 8.4 s (Rettenmeier et al., 2014).

https://doi.org/10.5194/wes-2020-104
Preprint. Discussion started: 24 September 2020

eawe european academy of wind energy
Open Access WIND ENERGY SCIENCE DISCUSSIONS

The recent work of Pettas et al. (2020), who combined a lidar simulator and a field reconstruction approach, showed that a 7-beam lidar can potentially increase the accuracy of reconstructed wind fields. For wake characterization, Doubrawa et al. (2016) indicated that the coverage of the scanning geometry is the key to adequately track the wake center location in time, and the scanning density to accurately estimate the velocity deficit distribution within the wake.

To evaluate the ability of currently available lidars to perform wake characterization, we select a few standard scanning configurations and use them to perform load validation within wakes. These are a 4-beam lidar (4P), an extended configuration with 7 beams, six arranged at the corner of a hexagon and a central beam (7P) (Pettas et al., 2020), the conical scanning lidar (Cone), the SL, and a general grid pattern (Grid) covering the full turbulence box (see Fig. 3).

The 4P and 7P patterns mimic measurements from a PL lidar obtained with a single scanning beam pointing at a fixed location, whereas the Cone, the SL and the Grid configurations mimic those from a CW lidar. Thus, a time lag between each sampling beam is simulated, and all the patterns are assumed to measure at the same single range. Although we do not optimize the scanning patterns, we use scan radii of about 70–80% of the rotor radius to estimate wind field characteristics based on previous recommendations (Dimitrov and Natarajan, 2017; Simley et al., 2018). Thus, we define the 4P, 7P, and Cone patterns accordingly. The SL trajectory is scaled to cover the full rotor area and the Grid pattern has a spatial resolution of 29 m. A preview distance of 0.7 D is assumed. Note that increasing the preview distance reduces the errors caused by the cross-contamination effects of the $v-$ and $w-$components, but raises errors due to the wind evolution (Simley et al., 2012) . More technical details on the scans are provided in Table 1. We assume a 2-s scan-period for all the simulated configurations, which refers to the time required for a beam to complete the full pattern. Given the finite resolution of the synthetic turbulence boxes (6.5 m in both lateral and vertical directions), the Cone and SL scanned locations are binned within the box grid, as reported in Table 1. A probe volume with an extension of 30 m in the LOS direction is assumed for all the analyzed patterns. We also define an additional case (Grid*) that neglects probe volume averaging effects.

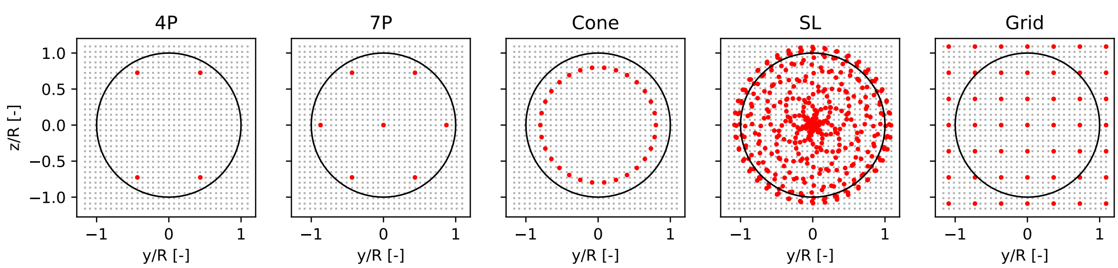

Figure 3. Selected lidar scanning patterns for the load analysis. The red markers indicate the scanned locations and the black dots in the background define the spatial resolution of the turbulence box. The rotor diameter is shown in a black solid line.

Table 1. Technical properties of the simulated lidar scanning configurations. Note that the Cone and SL measurements are binned according to the spatial resolution of the synthetic turbulence fields, thus leading to a reduction of the simulated scanning positions.

Scanning configuration	Measurements / scan (binned) [-]	Sampling frequency [Hz]	Scan period [s]	Measurements / 10-min [-]	Probe volume size [m]
4P	4	2	2	1200	30
7P	7	3.5	2	2100	30
Cone	100 (30)	50	2	9000	30
SpinneLidar (SL)	400 (93)	200	2	27900	30
Grid	49	25	2	14700	30
Grid*	49	25	2	14700	0

3.4 Wake field reconstruction techniques

A three-dimensional synthetic wake flow field, compliant with the DWM formulation, can be defined by a linear superposition of the ambient wind field and two turbulence terms as:

$$U_{wake}(x,y,z) = \bar{U}_{amb}(z) + u'_{i,K_{def}}(x,y,z) + u'_{j,K_{turb}}(x,y,z), \tag{5}$$

where $\bar{U}_{amb}(z)$ is the ambient wind speed including the atmospheric wind profile, $u'_{iK_{def}}(x,y,z)$ is a residual turbulence field with imposed wake deficits, and $u'_{j,K_{turb}}$ is a second turbulence field modelling wake-added turbulence effects. The subscripts i,j indicate two random field realizations. The $u'_{i,K_{def}}$ field can be computed as:

$$u'_{i,K_{def}}(x,y,z) = \bar{U}_{amb}(z)K_{def}(x,y,z) + u'_i(x,y,z) - \bar{U}_{amb}(z), \tag{6}$$

where K_{def} is the radial symmetric wake deficit time-series including a pre-computed stochastic meandering process calculated with the DWM model, and u'_i is a random turbulence realization from the Mann model with spectral properties as for the ambient wind field. The spectral properties of the turbulence are defined by $\alpha_k\epsilon^{2/3}, L, \Gamma$, which can be fitted based on freestream observations. The wind field formulation of Eqs. (5) and (6) is consistent with the domain of wind fields typically input to aeroelastic simulations. Finally, $u'_{j,K_{turb}}$ is obtained by simply scaling an isotropic turbulence field with low turbulence length scales, by the semi-empirical formulation in Eq. (19) in Madsen et al. (2010). By defining the $target$ wake flow fields with the DWM formulation, the underlying assumptions on which we define the wind field reconstruction techniques are:

1. The ambient wind conditions are known, including $\bar{U}_{amb}(z)$, the atmospheric turbulence intensity (TI_{amb}), and the atmospheric stability conditions (here implicitly prescribed through the Mann parameters: $\alpha_k\epsilon^{2/3}, L, \Gamma$).

2. The lidar-based wake fields can be reconstructed by incorporating lidar observations into a zero-mean, homogeneous and random Gaussian turbulence field generated by the Mann spectral tensor model.

3. The induction effects on lidar measurements are neglected and the Taylor's frozen turbulence hypothesis is assumed.

https://doi.org/10.5194/wes-2020-104
Preprint. Discussion started: 24 September 2020

4. The u-velocity fluctuations are recovered from the $target$ wake fields.

The corresponding random turbulence seeds from *set A* and *set B* have similar spectral properties, however, these fields only describe the turbulence structures in the freestream conditions. The lidar measurements of the wake field, combined with the reconstruction approach, should recover the whole information regarding the wake characteristics, including velocity deficits, wake-added turbulence and meandering in lateral and vertical directions. Further, the first assumption is not longer needed if a second instrument is deployed at the site measuring the freestream conditions (Borraccino et al., 2017; Peña et al., 2017). The second and third assumptions are inherent in the modelling approach and limitations of the DWM model, as well as other analytical wake models; however, the wake characteristics are extracted directly from the lidar observations rather than a physical-based deficit formulation. Eventually, wind turbine responses are mainly affected by the mean wind speed in the longitudinal direction (u-velocity) and its variance (Dimitrov et al., 2018), while the effects of the v- and w-turbulence are generally marginal (Dimitrov and Natarajan, 2017).

3.4.1 Constrained Gaussian field simulations (CS)

The algorithm for applying constraints on a zero-mean, homogeneous and isotropic Gaussian random field was developed in Dimitrov and Natarajan (2017). It uses a set of constraints that are here-derived from a virtual lidar simulator and an unconstrained random turbulence realization generated with the Mann spectral tensor model. Following the notation in Dimitrov and Natarajan (2017), we denote $\tilde{g}(\boldsymbol{r})$, where $\boldsymbol{r} = (x,y,z)$ is the spatial separation vector, an unconstrained random turbulence realization. The spectral property of $\tilde{g}(\boldsymbol{r})$ at each discrete lateral and vertical separation of the turbulence box can be computed from the Mann model in Eq. (2), given a set of parameters $(\alpha_k\epsilon^{2/3}, L, \Gamma)$. We denote a set of constraints as $\boldsymbol{H} = \{h_i(\boldsymbol{r}) = c_i, i, ..., M\}$, where each constraint is a measured time series for a particular spatial location $\boldsymbol{r}$ and M is the total number of constraints. The objective of the algorithm is to define a turbulence field $g(\boldsymbol{r})$, subjected to the constraints in $\boldsymbol{H}$ that maintains the covariance and coherence properties of the unconstrained field $\tilde{g}(\boldsymbol{r})$. As demonstrated in Dimitrov and Natarajan (2017), the unknown points of the field can be defined by maximizing their conditional probability distribution on the constraint set $\boldsymbol{H}$. Thus, we define the residual field $\xi(\boldsymbol{r}) = g(\boldsymbol{r}) - \tilde{g}(\boldsymbol{r})$, which is the difference between the constrained and unconstrained fields. This is also a random Gaussian field, where its values at the constraint locations are known $\xi(\boldsymbol{r_i}) = c_i - \tilde{g}(\boldsymbol{r})$. The values of the residual field at unknown locations can be derived as:

$$\bar{\xi}(\boldsymbol{r}) = \langle \xi(\boldsymbol{r}) | \boldsymbol{H} \rangle = \boldsymbol{\zeta}(\boldsymbol{r}) \boldsymbol{Z}^{-1} (\boldsymbol{H} - \tilde{g}(\boldsymbol{r})), \tag{7}$$

where $\langle . \rangle$ denotes ensemble averaging, $\boldsymbol{\zeta}(\boldsymbol{r})$ is a vector of cross-correlations between the constraints and the field, and $\boldsymbol{Z}$ is the symmetric correlation matrix of the constraints set. Both $\boldsymbol{\zeta}(\boldsymbol{r})$ and $\boldsymbol{Z}$ can be computed from Eq. (3). Eventually, any constrained realization can be written as a sum of the unconstrained field and the mean of the residual field as:

$$g(\boldsymbol{r}) = \tilde{g}(\boldsymbol{r}) + \boldsymbol{\zeta}(\boldsymbol{r}) Z^{-1} (\boldsymbol{H} - \tilde{g}_r(\boldsymbol{r})). \tag{8}$$

By denoting $u'_{\mathrm{CS,B,i}} = g(\boldsymbol{r})$, as the constrained turbulence field that incorporates lidar measurements into a random turbulence realization i from *set B*, we can derive the reconstructed wake flow field to be input in aeroelastic simulations as:

$$U_{\mathrm{CS}}(x,y,z) = \bar{U}_{amb}(z) + u'_{\mathrm{CS,B,i}}(x,y,z). \tag{9}$$

Note that the accuracy of the resulting wind field will depend on the fidelity and accuracy of the measurements used to characterize the wake deficit.

3.4.2 Wake deficit superposition simulations (WDS)

The wake deficit superposition approach (WDS) assumes that velocity deficits can be described by a bivariate Gaussian shape function, which is fitted based on lidar measurements of the $target$ wake flow field. Several studies have demonstrated the viability and robustness of the Gaussian curve fitting to track wake deficit displacements in the far-wake region (Trujillo et al., 2011; Reinwardt et al., 2020). In our study, the wake shape function not only tracks the wake meandering, but it is used to quantify the depth and width of the wake at each quasi-instantaneous scan performed by the lidar. Thus, following the notation of Trujillo et al. (2011), we define the lidar-estimated 'instantaneous' wake deficit $K_{def,lidar}$ as:

$$K_{def,lidar}(x,y,z) = \frac{U_{amb}(z) - U_{lidar}(x,y,z)}{U_{amb}(z)} = \frac{A}{2\pi\sigma_{wy}\sigma_{wz}} \exp\left[-\frac{1}{2}\left(\frac{(y_i-\mu_y)^2}{\sigma_{wy}^2} + \frac{(z_i-\mu_z)^2}{\sigma_{wz}^2}\right)\right], \tag{10}$$

where (μ_y, μ_z) define the wake center location, $(\sigma_{wy}, \sigma_{wz})$ are width parameters of the wake profile in the y and z directions, respectively, (y_i, z_i) denote the spatial location of the LOS and A is a scaling parameter dictating the depth of the wake. As discussed above, we assume that U_{amb} is known, while the lidar measurements in the wake (U_{lidar}) are sampled by the lidar simulator. The optimal wake parameters are obtained from a least-squares fitting procedure, which is performed for each completed scanning period ($\sim$ 2 s as described in Table 1). Finally, the lidar-fitted wake deficits are superimposed on a random turbulence field realization from *set B*. A preliminary analysis shows that wide turbulence boxes (208 m $\times$ 208 m) can present large turbulence structures within, i.e., broad regions across the box characterized by low wind speeds, whose sizes can alter the depth and width properties of the lidar-fitted wake deficits in Eq. (10). It follows that the wake properties of the reconstructed field can considerably deviate from the actual imposed wake characteristics. To compensate for these deviations, we fit a second Gaussian shape function ($K_{def,\mathrm{WDS}}$) as that from Eq. (10), which accounts for the turbulence structures within the random turbulence box from *set B*, by reformulating the deficits as:

280 $$K_{def,lidar}(x,y,z) = \frac{U_{amb}(z) - U_{WDS}(x,y,z)}{U_{amb}(z)} = \frac{U_{amb} - (U_{amb}(z)K_{def,\mathrm{WDS}}(x,y,z) + u'_{B,i}(x,y,z))}{U_{amb}(z)}, \tag{11}$$

where U_{WDS} is the WDS-reconstructed wake field, which can be defined as a linear summation of the ambient wind field U_{amb} scaled by the fitted wake function $K_{def,WDS}$, and the random turbulence realization $u'_{B,i}$. This formulation is consistent with that of the DWM model in Eq. (6). As the sampling frequency of the lidar is lower than the sampling frequency of the synthetic wind field, we interpolate the fitted wake characteristics at each scan to the whole turbulence field by applying a nearest-neighbor interpolation scheme. Finally, the reconstructed wake field input to aeroelastic simulations is defined by:

$$U_{\mathrm{WDS}}(x,y,z) = \bar{U}_{amb}(z)K_{def,\mathrm{WDS}}(x,y,z) + u'_{B,i}(x,y,z). \tag{12}$$

https://doi.org/10.5194/wes-2020-104
Preprint. Discussion started: 24 September 2020

4 Results

The results are presented in three main parts. Firstly, we assess the accuracy of lidar-reconstructed wake fields against $target$ fields in Sect. 4.1. Secondly, we carry out the load validation analysis in Sect. 4.2, and separately present the load predictions uncertainty relative to the CS-approach in Sect. 4.2.2 and that of the WDS-approach in Sect. 4.2.3. A more detailed analysis of the predicted load time-series and load spectral properties is conducted in Sects. 4.2.4 and 4.2.5. Finally, we evaluate the sensitivities of atmospheric turbulence conditions as well as selected lidar technical specifications on the load predictions accuracy in Sect. 4.3.

4.1 Uncertainty of reconstructed wake fields

In this section, we evaluate the accuracy of the lidar-reconstructed fields against $target$ fields. At first, we assess the accuracy of the u-velocity component time-series, by computing the root mean square error, RMSE $= \sqrt{1/n\sum_i^n(\tilde{y}_i - \hat{y}_i)^2}$, between the reconstructed $(\tilde{y})$ and $target$ velocity $(\hat{y})$, where n = 8192 is the grid size of the box in the time direction, normalized over the mean $target$ velocity at each grid point of the turbulence box. Then, we derive a measure of the 'explained' variance by the lidar measurements. The explained variance ratio (ρ_E^2) is defined in Dimitrov and Natarajan (2017) as the proportion of the variance in the actually measured field that is transferred to the unconstrained field by imposing the constraints. This is computed as the square of the cross-correlation coefficient $\rho_E^2 = (\mathrm{cov}(\tilde{y},\hat{y})/\sigma_{\tilde{y}}\sigma_{\hat{y}})^2$, between reconstructed $(\tilde{y})$ and $target$ $(\hat{y})$ wind speed fluctuations at each grid point. As the $target$ and reconstructed fields are based on two random uncorrelated turbulence seeds, $\rho_E^2 \sim 0$ is expected across the box, if no lidar information was included. Contrarily, $\rho_E^2 = 1$ indicates that the reconstructed time-series is fully-correlated with the $target$, thus the variance of the reconstructed field matches that of the $target$ field.

Figure 4 shows the spatial distribution of the normalized RMSE and ρ_E^2 derived from the CS- and WDS-reconstructed fields, with the 7P, Cone and Grid configurations (see Table 1 for specifications). For this particular analysis, the simulations are run at the downstream distance of 5 D, where D = 179 m is the diameter of the DTU 10 MW turbine, and ambient conditions characterized by U_{amb} = 6 m/s, TI$_{amb}$ = 8 %. The atmospheric vertical wind profile is defined by a power law model with shear exponent of 0.2. It can be seen that the locations of the imposed constraints are characterized by the lowest RMSE and highest ρ_E^2. This effect is more pronounced for the CS results, as the algorithm imposes the actual observations directly in the synthetic field. The RMSE would tend to zero, if the length of probe volume is neglected, the lidar's sampling frequency corresponds to the sampling frequency of the wind field, and cross-contamination effects are compensated. It can also be observed that the RMSE increases (and ρ_E^2 decreases) for spatial regions that are farther from the lidar's beams. This occurs due to the covariance structure of the unconstrained field, for which the unknown points are nearly uncorrelated with the imposed constraints. The errors introduced by the WDS-fields are partly a consequence of an erroneous estimation of the wake deficit parameters (i.e. due to the limited spatial scanning configuration), and due to the small-scale turbulence structures contained in the turbulence box. Finally, the results of Fig. 4 confirms that the spatial resolution of the scanning patterns has a significant impact on the

https://doi.org/10.5194/wes-2020-104
Preprint. Discussion started: 24 September 2020

accuracy of the reconstructed fields. Therefore, patterns that cover a larger region of the rotor can lead to more accurate field
320 representations (Dimitrov and Natarajan, 2017; Pettas et al., 2020).

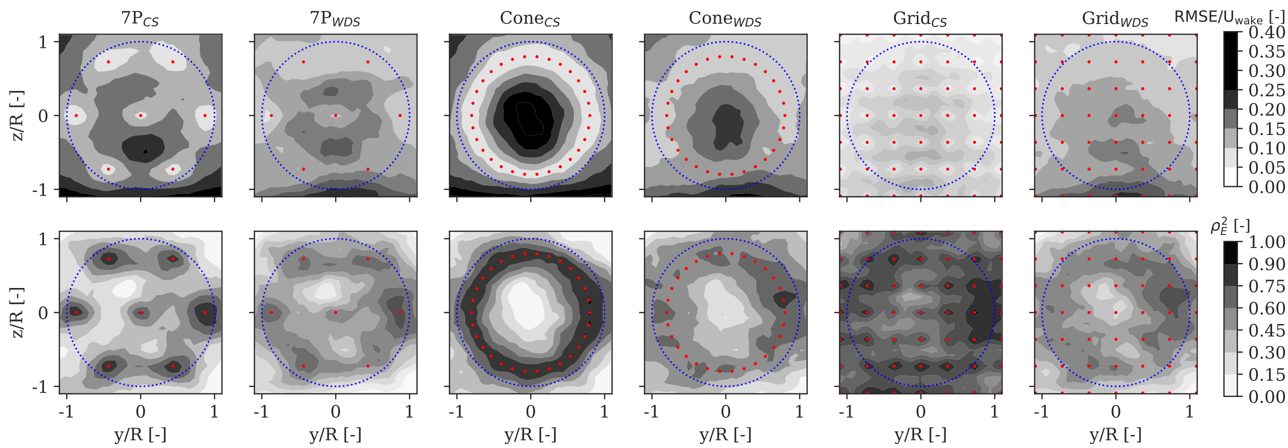

Figure 4. Error visualization of the CS- and WDS-reconstructed fields for selected scanning configurations. The top row refers to the RMSE normalized over the $target$ velocity at each grid point. The bottom row refers the explained variance ratio. The red markers identify the centers of the lidar beam sampling volumes. The wind turbine rotor is shown in blue.

In Fig. 5, we show a comparison of the lidar-reconstructed u-velocity time-series extracted at hub height, using the Grid pattern, with the $target$ observations derived at the same location. The $target$ wake field is simulated with U_{amb} = 6 m/s and TI$_{amb}$ = 8 %. The time-series of the virtual lidar measurements is also shown. It is seen that both field reconstruction approaches can predict the reduced wind speed observed in the wake region as well as recover in details the wind speed
325 fluctuations of the $target$ field. However, uncertainty is introduced due to the limited lidar sampling frequency, the length of the probe volume (here assumed of 30 m) and by the adopted field reconstructing approaches. The results of Fig. 5 demonstrate that incorporating lidar data directly in the reconstructed field (i.e. CS-approach) leads to reproducing more accurate fields compared to the WDS-approach.

In addition, we compute the power spectral density (PSD) of the above analyzed u-velocity fluctuations for a 10-min simu-
330 lation, and compare the results in Fig. 6. We observe that the PSD of the reconstructed fields is comparable to that of the $target$ for frequencies up to $\approx$ 1 Hz, while the energy spectral content at higher frequencies is considerably attenuated. According to the definition in Larsen et al. (2008), the dominant frequency of the wake meandering is defined as $f_{cut,off} = U/(2D)$, which results in 0.016 Hz ($\sim$ 62 s period). As the lidar completes a full-scan in about 2 s, the large-scale wake meandering dynamics are well-captured. Further, as the wake meandering is the main source of wake added turbulence (i.e. u-component
335 variance), the energy spectral content in the low frequency range is recovered. The enhanced turbulent energy content in the high-frequency range (> 1 Hz), observed in the $target$ field, originates from the small-scale wake added turbulence (Madsen et al., 2010; Chamorro et al., 2012). These effects are not fully recovered in the reconstructed fields, mainly due to the lidar

https://doi.org/10.5194/wes-2020-104
Preprint. Discussion started: 24 September 2020

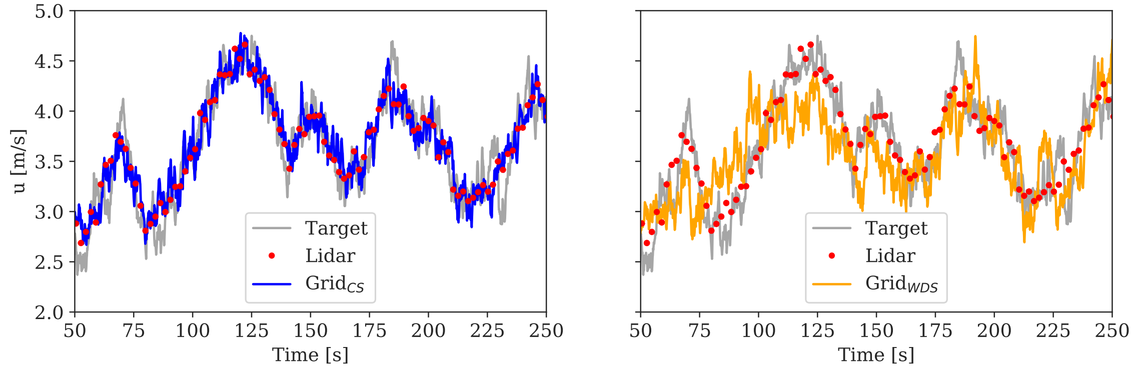

Figure 5. Comparison between the *target* u-velocity time-series at hub height (grey solid line) and the reconstructed field based on the CS-approach (left) and WDS (right) extracted at hub height. The lidar data are shown in red. The *target* simulations are run with U_{amb} = 6 m/s and TI$_{amb}$ = 8 %.

probe volume and limited sampling frequency. Nevertheless, the contribution of these sources of uncertainty on the power and load prediction accuracy is the subject of this study.

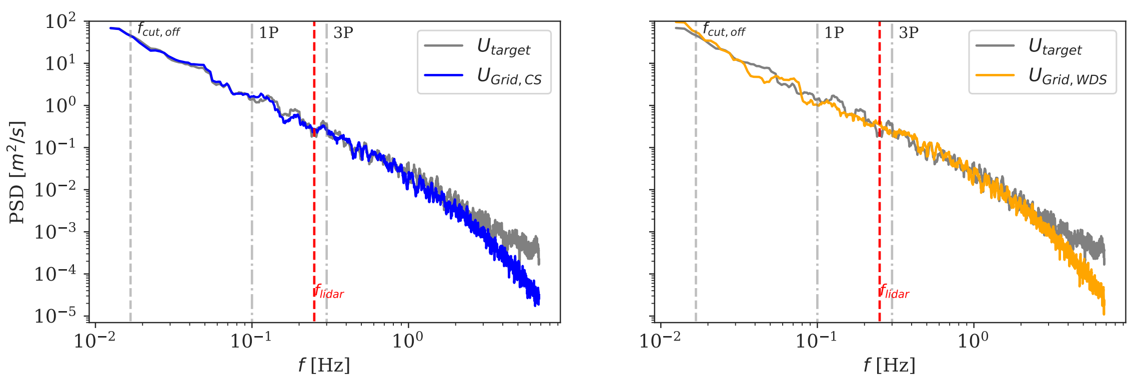

Figure 6. Comparisons of the power spectra density (PSD) of the *target* u-velocity component measured at hub-height with predictions obtained by the CS-field (left), and the WDS-field (right). The dominant frequency of the wake meandering $f_{cut,off}$ ≈ 0.016 Hz, the rotational frequency of the rotor and its harmonics (1P ≈ 0.1 Hz and 3P ≈ 0.3 Hz), and the Nyquist frequency of the lidar (≈ 0.25 Hz) are shown (see text for more details).

https://doi.org/10.5194/wes-2020-104
Preprint. Discussion started: 24 September 2020

4.2 Load validation

The DTU 10 MW reference wind turbine is used for the load validation analysis (Bak et al., 2013). The load simulations are carried out using the aeroelastic code HAWC2 (Larsen et al., 2007) and inflow wind conditions measured from an offshore site, as described in the next section (Sect. 4.2.1). Note that we run the analysis based on offshore wind conditions, which are characterized by low turbulence, thus wake effects are more prominent. This work evaluates the load prediction accuracy at the main wind turbine structures, such as blades, shaft and tower. Therefore, we neglect the modelling of the offshore substructures and foundations, and we use the onshore model of the DTU 10 MW. Following the load validation procedure described in Sect. 2, we quantify the uncertainty of resulting load predictions from the *baseline*, *CS* and *WDS* simulations against results obtained with the *target* fields. The CS and WDS simulations are evaluated for the analyzed lidar configurations of Fig. 3, i.e., the 4P, 7P, Cone, SL, Grid and Grid* patterns with parameters provided in Table 1. Thus, the following uncertainty indicators are calculated:

- Bias: $\Delta_R = E(\tilde{y})/E(\hat{y})$
- Uncertainty: $X_R = \sqrt{\langle(\tilde{y}/\hat{y} - E(\tilde{y})/E(\hat{y}))^2\rangle}$

where the symbol $E(.)$ denotes the mean value and $\langle.\rangle$ the ensemble average, $\hat{y}$ is the quantity of interest (i.e. power or load statistics) derived from the *target* simulations, and $\tilde{y}$ corresponds to that produced by the reconstructed fields. We evaluate Δ_R and X_R on the resulting 10-min power and load statistics and provide results in Sect. 4.2.2 for the CS-fields, and in Sect. 4.2.3 for the WDS-fields. The analyzed wind turbine responses include mean power production levels ($\mathrm{Power_{mean}}$), and fatigue loads. We make use of the rainflow counting algorithm to compute the 1-Hz damage equivalent fatigue loads with a Wöhler exponent of m = 12 for blades and m = 4 for steel structures as tower and shaft. Thus, we compute fatigue loads at the blade root flapwise and edgewise moments $\mathrm{MxBR_{DEL}}, \mathrm{MyBR_{DEL}}$, tower-bottom fore-aft and side-side $\mathrm{MxTB_{DEL}}, \mathrm{MyTB_{DEL}}$, the torsional loads at the tower top (also referred to as yaw moment) $\mathrm{MzTT_{DEL}}$ and torsional loads at the drivetrain $\mathrm{MzSh_{DEL}}$. Furthermore, we quantify the accuracy of the reconstructed wake fields based on estimates of the rotor-effective wind speed (U_{eff}), defined as the weighted sum of the u-velocity measured across the rotor area, the explained variance ratio ρ_E^2 and the u-velocity variance σ_u^2 computed from the reconstructed turbulence boxes. Finally, a load time-series and spectral analysis is conducted in Sects. 4.2.4 and 4.2.5.

4.2.1 Site conditions

Load simulations are carried out using site-specific observations collected from the FINO1 meteorological mast installed at the German offshore wind farm Alpha Ventus. The wind farm is situated in the North Sea and about 45 km north of the island of Borkum (Kretschmer et al., 2019). Data were collected over a period of three years from 2011 to 2014 and details can be found in Kretschmer et al. (2019). In the present work, we only make use of wind speeds and turbulence intensities measured from a 90 m sonic anemometer installed at the mast. Thus, we extract mean turbulence intensity values binned for wind speeds ranging between 6 m/s and 22 m/s, under near-neutral conditions, and use these statistics as inputs for the load validation analysis. We

https://doi.org/10.5194/wes-2020-104
Preprint. Discussion started: 24 September 2020

use 18 turbulence seeds (the IEC recommends at least 6 seeds) for each wind speed in the range of 6–22 m/s, with a wind speed step of 2 m/s, and corresponding turbulence intensities of 8, 7, 7, 6, 6, 6, 6, 5, 5 %, leading to 162 simulations for each analyzed scanning configuration. Simulations with ambient wind speeds below 6 m/s are disregarded, as the wind speed approaching the rotor drops below the turbine's cut-in threshold, due to wake deficit effects, and the turbine shuts down. Note that the recorded turbulence estimates at Alpha Ventus are considerably lower (approximately a factor of 3) than values recommended by the low turbulence IEC-class C. Thus, we perform the load validation on more realistic turbulence estimates characterizing offshore sites, since IEC-class C conditions would significantly attenuate the wake-induced effects, as higher ambient turbulence leads to a faster recovery of the wake deficit. We use standard IEC-recommended turbulence model parameters ($L = 29.4$ m and $\Gamma = 3.9$). The parameter $\alpha_k \epsilon^{2/3}$ is fitted to obtain the $target$ turbulence levels in each simulation. The atmospheric wind profile is described by a power-law with fixed shear exponent of $\alpha = 0.2$, as recommended in the IEC standard. The spacing between the analyzed and upstream turbines is fixed at 5 D. Although we run the load validation procedure on selected nominal parameters, we investigate the sensitivity of the main load-driver parameters in a separate section (see Sect. 4.3).

The $target$ wake field characteristics resulting from the 162 simulations are shown in Fig. 7. It is seen that the wake considerably reduces the inflow wind speed approaching the rotor (i.e. U_{eff}) by approximately 35%, compared to the ambient wind speed. This effect decreases for higher winds (>14 m/s) due to the low thrust coefficients of the turbine. Further, the turbulence in the wake is nearly doubled at low wind speeds compared to ambient conditions. Finally, the wake meandering statistics computed as the standard deviation of the wake center displacements in the transversal directions normalized on the rotor diameter (σ_{μ_y}/D and σ_{μ_z}/D) are also shown.

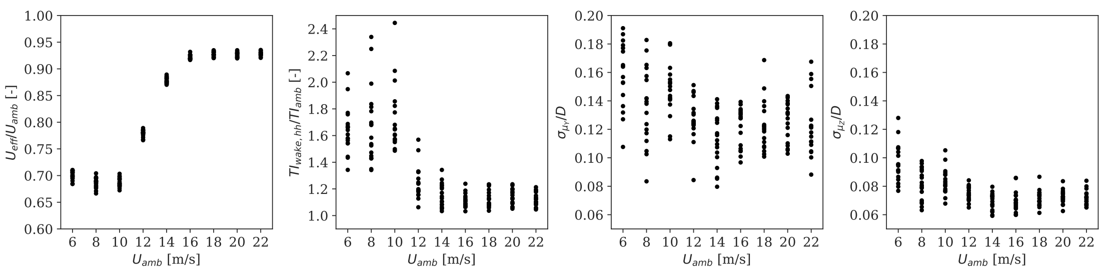

Figure 7. Scatter plots of the 10-min wake field characteristics resulting from the 162 simulations used as $target$ in the load analysis. The parameter $TI_{wake,hh}$ refers to the turbulence intensity measured at hub-height in the wake; σ_{μ_y}/D is a measure of the amplitude of wake meandering in the lateral direction and σ_{μ_z}/D refers to the vertical displacement of the wake.

4.2.2 Load uncertainty of constrained Gaussian wake field simulations (CS)

The uncertainties Δ_R and X_R of the load predictions obtained with the CS-fields as function of the ambient wind speed are shown in Fig. 8. It is found that the biases largely vary depending on the simulated scanning pattern and analyzed load sensor. First, we can observe that patterns with fewer 'points' (i.e., 4P, 7P and Cone) overestimate U_{eff} by 2–10% (see Fig. 8a). This is

https://doi.org/10.5194/wes-2020-104
Preprint. Discussion started: 24 September 2020

because 1) these patterns have insufficient spatial resolution to fully characterize the wake flow; 2) the autocorrelation structure of the unconstrained turbulence box is such that the spatial regions that are not scanned by the lidar are nearly uncorrelated with the locations of the imposed constraints. Thus, the reconstructed wind speed, in the regions that are not scanned by the lidar, approaches the ambient wind speed values. Therefore, lower deficits are simulated or equivalently higher rotor-effective wind speeds are predicted. As a consequence, the power predictions are overestimated (Δ_R >10%), as seen for ambient wind speeds below 14 m/s in Fig. 8b. Patterns with high spatial resolution, as the SL, Grid and Grid*, provide rotor-effective wind speed and power production estimates in good agreement with the $baseline$.

The statistics of ρ_E^2 in Fig. 8c indicate that increasing the spatial resolution of the pattern (see SL, Grid and Grid*) leads to a more accurate reconstruction of the wake turbulence. The biases of both ρ_E^2 and U_{eff} decreases for high wind speeds, due to the attenuated wake-induced effects (see Fig. 7). The improved performance of the SL, Grid (and Grid*) is also confirmed by the estimates of σ_u^2 in Fig. 8d, which show that the SL and Grid configurations can match the $target$ variance with an accuracy up to 98%, compared to 40–60% estimates inherent of the 4P, 7P and the Cone configurations. Nevertheless, the observed biases of U_{eff}, ρ_E^2 and σ_u^2 reveal that the 4P, 7P and Cone patterns lead to inaccurate wake field representations and do not satisfy the criteria of the load validation (see Criteria I in Sect. 2).

The results from simulations with the SL, Grid and Grid* patterns provide fatigue load statistics of $\mathrm{MxBR_{DEL}}$, $\mathrm{MxTB_{DEL}}$, $\mathrm{MzTT_{DEL}}$ and $\mathrm{MzSh_{DEL}}$ in good agreement with the results of the $baseline$ (see Fig. 8e–h). However, the calculated biases indicate a consistent underprediction at all wind speeds. This gap is largely compensated when probe volume effects are neglected, as seen for the Grid* (green lines). Overall, the observed deviations in the load predictions are due to the uncertainty of lidar measurements (i.e. size of the probe volume, cross-contamination effects, limited sampling frequency), and the limited scanning coverage of the patterns.

Figure 9 shows the statistics of Δ_R and X_R including all wind speeds. As expected, the $baseline$ leads to $\Delta_R \sim 1$ for all the analyzed load sensors, which indicates that the adopted 18 turbulence seeds are sufficient for the load statistics to converge. The large biases from simulations with the 4P, 7P and Cone patterns (Δ_R ~0.87–1.37) follow from the inaccurate wind field reconstruction discussed above. The load predictions with the SL and the Grid configurations provide biases closer to the $baseline$, although turbulence-driven load sensors are underpredicted by 2–7%. These deviations decrease as probe volume effects are neglected (i.e. $\Delta_R \sim 1\%$ for Grid* in Fig. 9-left), which shows the dependency of the load prediction accuracy on the probe volume size.

The statistics of X_R are shown in Fig. 9-right. The $baseline$'s X_R is a direct measure of the statistical uncertainty intrinsic of the DWM model, which is due to the stochastic properties of the synthetic turbulence field and wake meandering. Thus, the turbine responses that are largely affected by wake-induced effects are identified by high X_R values (see $baseline$ in Fig. 9-right). The power predictions as well as the majority of fatigue loads show a relatively high statistical uncertainty ($X_R \sim$ 0.05–0.09), resulting in a large load scatter. The X_R values of MyTB and MzSh are significantly higher than other load sensors. The cause of the former is structural resonance occurring at low wind speeds that excites the tower natural frequency. This effect originates from a design aspect of the DTU 10 MW turbine and it is independent of the wake-field reconstructing approach. The cause of the latter is the intense controller activity to regulate the generator torque under high-variable inflow conditions.

https://doi.org/10.5194/wes-2020-104
Preprint. Discussion started: 24 September 2020

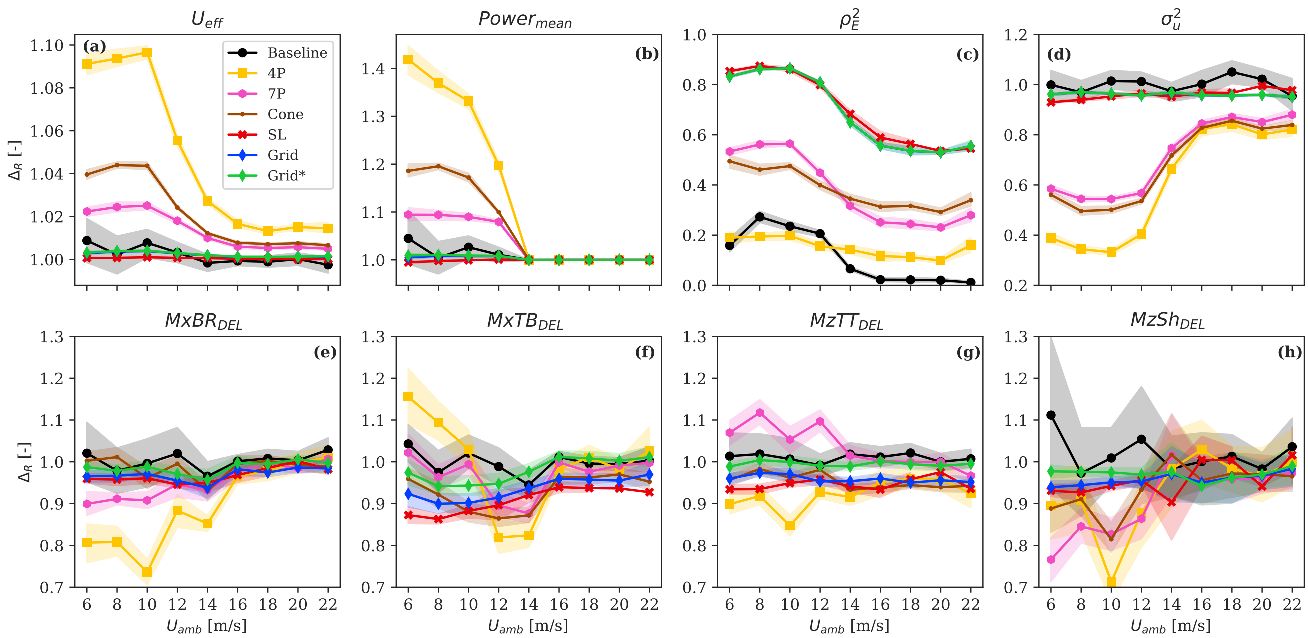

Figure 8. Comparison of bias Δ_R (solid line) and uncertainty X_R (error band) of selected load sensors as function of the ambient wind speed. The uncertainty indicators are computed against the $target$ observations, for each ambient wind speed (marker) that consists in 18 aeroelastic simulations with random turbulence seeds. The lidar-based results are derived from simulations with CS-fields.

The CS-based load predictions are characterized by significantly lower X_R values compared to the statistics obtained with the $baseline$. Indeed, X_R is reduced by a factor between 1.4–5 for the main wind driven turbine responses such as $\mathrm{Power_{mean}}$, and fatigue loads (i.e. $\mathrm{MxBR_{DEL}}$, $\mathrm{MxTB_{DEL}}$, $\mathrm{MzTT_{DEL}}$ and $\mathrm{MzSh_{DEL}}$). The CS-fields, reconstructed using a sufficiently resolute scanning pattern and with limited lidar probe volume can therefore satisfy both the load validation criteria stated in Sect. 2.

4.2.3 Load uncertainty of wake deficit superposition simulations (WDS)

We present the results relative to the WDS simulations in the same fashion as done for the CS in Sect. 4.2.2. Thus, we plot the load predictions uncertainty as function of the ambient wind speeds in Fig. 10. It can be noticed that the 4P, 7P and Cone patterns lead to improved biases of U_{eff}, and consequently $\mathrm{Power_{mean}}$ (see Fig. 10a,b), compared to the results obtained with the CS fields (see Fig. 9). Indeed, the $\mathrm{Power_{mean}}$ predictions computed with the WDS-approach and the 7P pattern are comparable with the $baseline$, while the corresponding results with the CS-fields produced an overprediction of 10%. In addition, improved estimates of both ρ_E^2 and σ_u^2 are seen in Fig. 10c,d, which indicates a more accurate reconstruction of the wake turbulence by the WDS- than the CS-approach. These findings suggest that, for patterns with low spatial resolution, more information of the wake characteristics can be recovered by fitting a generic wake shape function rather than incorporating lidar

https://doi.org/10.5194/wes-2020-104
Preprint. Discussion started: 24 September 2020

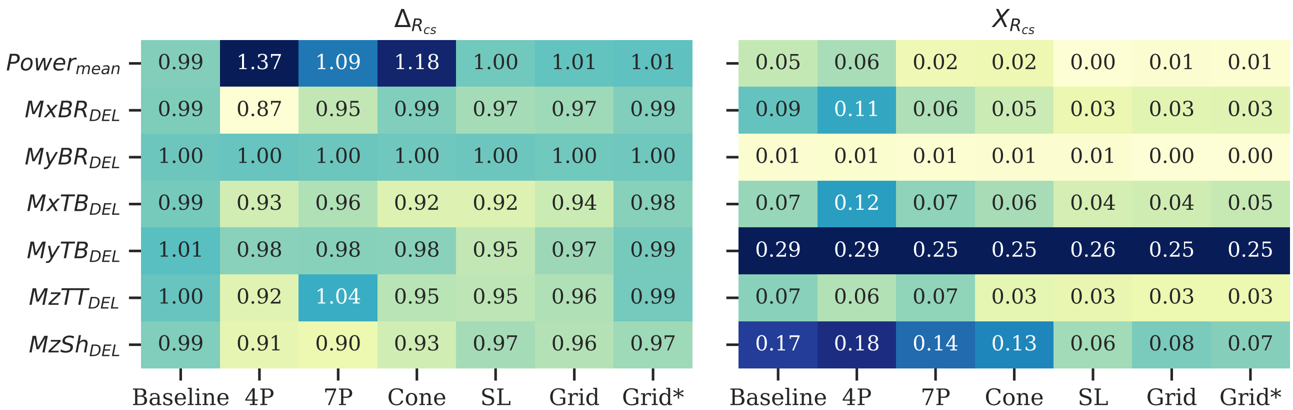

Figure 9. Uncertainty indicators of the load validation analysis based on the constrained field simulations (CS). Results are tabulated according to the load components and lidar scanning patterns. The color-map reflects the amplitude of the error, thus a dark blue identifies an overprediction while the ligth-green indicates an undeprediction. A perfect statistical prediction leads to $\Delta_R = 1$ and $X_R = 0$.

measurements directly into the turbulence boxes. Overall, simulations with the 7P, SL, Grid and Grid* patterns can produce power predictions comparable with the $baseline$ (see Fig. 10b), whereas the 4P and Cone lead to inaccurate predictions. Figure 10e – h shows that the fatigue loads obtained with the 7P, SL, Grid and Grid* configurations are generally lower than that from the $baseline$.

We quantify the statistics of Δ_R and X_R including all the wind speeds with WDS-simulated fields, and present the results in Fig. 11. As discussed above, the 4P and Cone patterns overpredict the rotor-effective wind speed and underpredict the wake turbulence; these effects counteract each other leading to fictitious biases of fatigue loads. Similar conclusions can be made for the 7P configuration, although it provides reliable power estimates. As seen for the CS-results, the SL, Grid and Grid* configurations provide biases in good agreement with the $baseline$, although fatigue loads are underpredicted by $\Delta_R \sim$ 2–3%. By neglecting the volume-averaging effects (see Grid*), only a marginal improvement of the biases is achieved. Simulations with the WDS-fields can reduce the statistical uncertainty of $\mathrm{Power_{mean}}$ by a factor of 5, and the main load components (i.e. $\mathrm{MxBR_{DEL}}$, $\mathrm{MxTB_{DEL}}$, $\mathrm{MzTT_{DEL}}$ and $\mathrm{MzSh_{DEL}}$) by a factor of 1.2–2 compared to the $baseline$ (see X_R in Fig. 11-right).

4.2.4 Time-series analysis of load predictions

In this section, we investigate the accuracy of lidar-reconstructed load time-series against $target$ observations. An illustrative example is provided in Fig. 12, where the lidar-based power and loads time-series predictions are compared with the $target$ simulations. It is observed that both CS- and WDS-approaches can recover to a large extent wake-induced effects, and the instantaneous events on the wind turbine responses, leading to load time-series that are highly correlated with the $target$ observations. This finding explains the reductions of X_R observed in Figs. 9 and 11.

https://doi.org/10.5194/wes-2020-104
Preprint. Discussion started: 24 September 2020

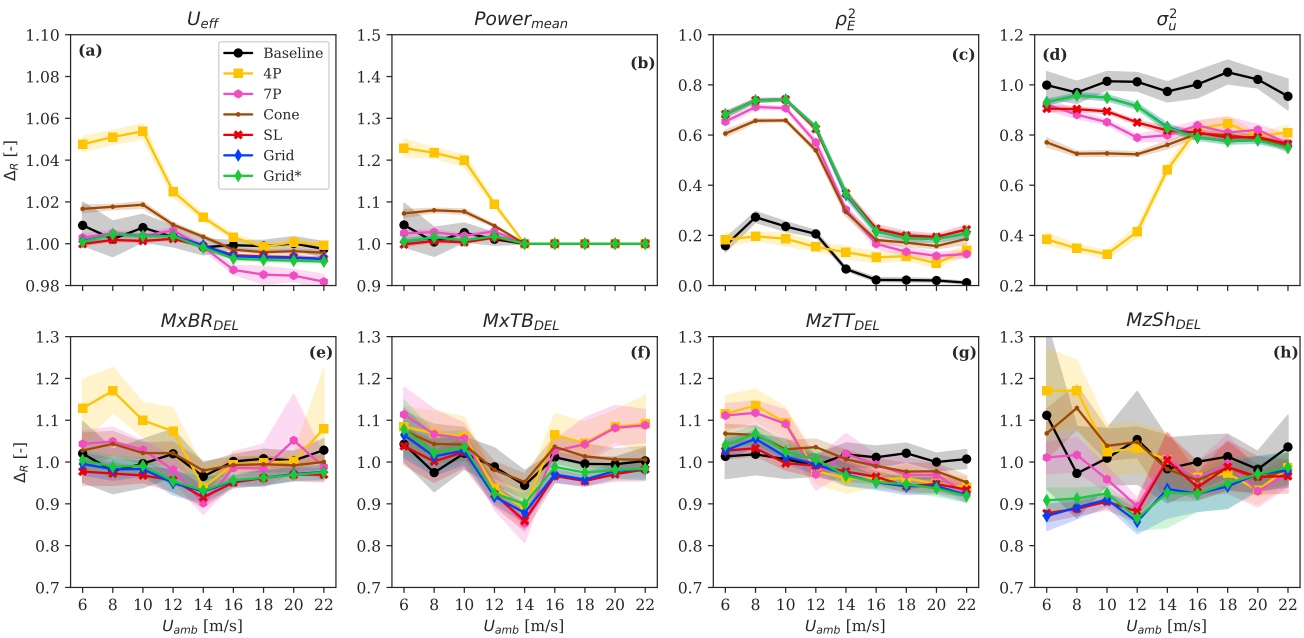

Figure 10. Similar to Fig. 8 but for WDS fields.

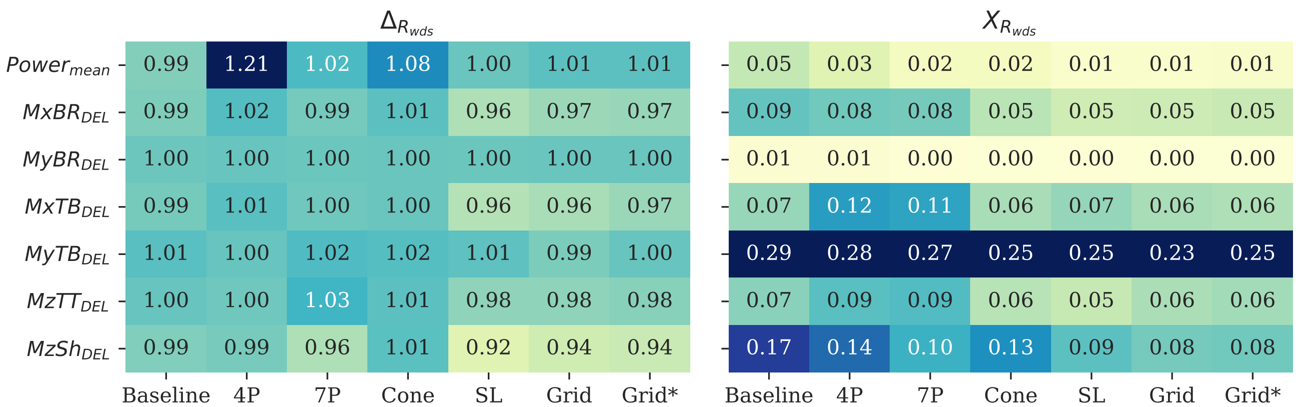

Figure 11. Similar to Fig. 9 but for WDS fields.

In order to quantify the accuracy of the predicted load time-series, we evaluate the cross-correlations measure $\rho(\tilde{y},\hat{y}) = \mathrm{cov}(\tilde{y},\hat{y})/\sigma_{\tilde{y}}\sigma_{\hat{y}}$, between the lidar-based results $(\tilde{y})$ and the $target$ simulations $(\hat{y})$ (ρ = 1 means perfect correlation). We focus the analysis on the SL, Grid and Grid* configurations, which provide the most promising results, as demonstrated in the previous sections. We compute ρ for all the 162 simulations and for each load component, and provide average estimates in
465 Fig. 13. It is found that both the CS- and WDS-predicted $\mathrm{Power_{mean}}$ time-series reach a nearly perfect correlation with the

https://doi.org/10.5194/wes-2020-104
Preprint. Discussion started: 24 September 2020

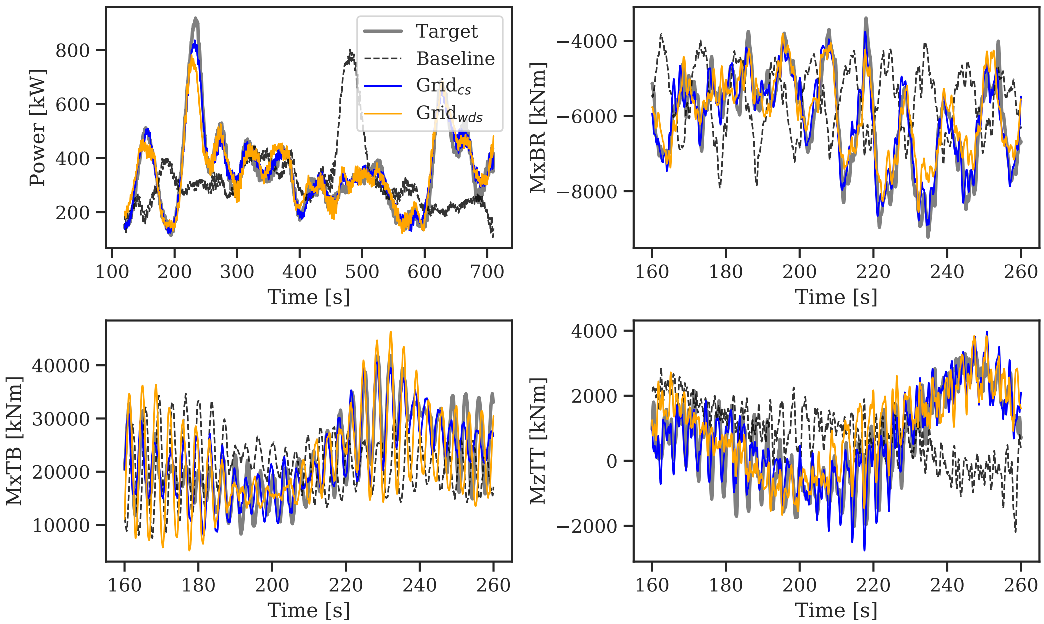

Figure 12. Comparison of predicted load time-series based on aeroelastic simulations carried out with the $target$, $baseline$, CS- and WDS-reconstructed fields. The lidar-based fields are reconstructed using the Grid pattern.

actual $target$ observations ($\rho = 0.96$–0.99). Note that $\mathrm{Power_{mean}}$ is a low frequency signal (see Fig. 12a), which is marginally affected by the local turbulence fluctuations. A high correlation value is also obtained for MxBR ($\rho = 0.89$–0.98), and for the tower top and shaft load components ($\rho = 0.60$–0.90). The correlation relative to MxTB drops to ≈ 0.33 with the WDS-simulations, while higher values are achieved by the CS results. It should be noted that the structural resonance occurring at low wind speeds, which excites the tower can potentially affect the correlation results. It can be seen from Fig. 12 that the MxTB time-series presents a nearly periodic signal, where the wind turbulence imprint is marginal. Overall, the accuracy of lidar-reconstructed load time-series show a significantly higher degree of correlation with the $target$ observations, compared to that achieved by the $baseline$. Furthermore, the CS-approach can predict more accurately the observed load fluctuations compared to the WDS-approach.

4.2.5 Spectral coherence analysis of load predictions

We conduct a spectral analysis on the time-series of MxBR, MxTB, and MzTT, which are highly correlated with the wake meandering (Muller et al., 2015; Moens et al., 2019; Ning and Wan, 2019) and are largely affected by the wake turbulence. The PSD analysis is provided in Appendix A, and shows that neither of the field reconstruction methods shifts the energy content among frequency nor introduce instabilities (i.e. artificial artifacts).

https://doi.org/10.5194/wes-2020-104
Preprint. Discussion started: 24 September 2020

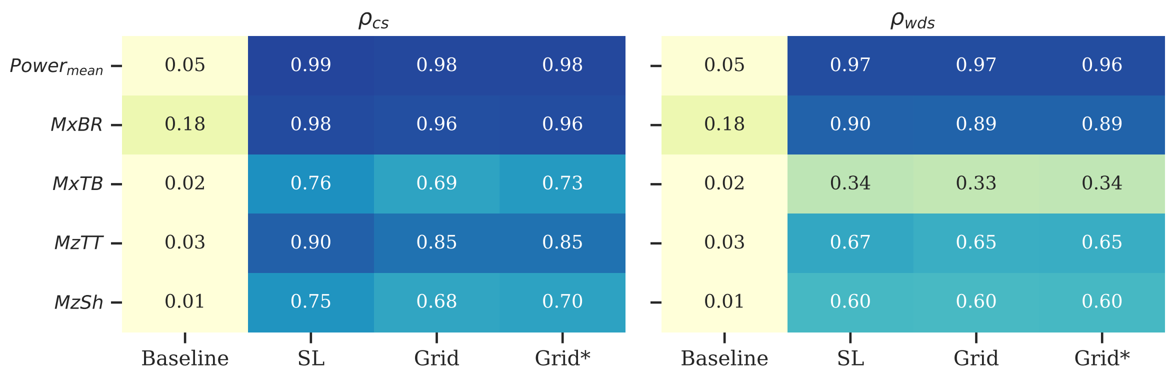

Figure 13. Average cross-correlation coefficient (ρ) computed between the reconstructed and $target$ load times-series from all the 162 simulations. Results from the CS-fields are shown in the left panel, and that from the WDS-fields in the right.

The spectral coherence analysis provides more insight on the accuracy of reconstructed blade and tower loads. Here, we compute the coherence as $\gamma = |S(\tilde{y},\hat{y})(f)|/(S(\tilde{y})(f)S(\hat{y})(f))$, where $S(\tilde{y})$ and $S(\hat{y})$ are the auto-spectra of the CS (or WDS) and $target$ load estimates, and $S(\tilde{y},\hat{y})$ is their cross-spectrum. We compare the coherence resulting from the load time-series produced by either CS and WDS simulations and the $target$ observations, at U_{amb} = 6 m/s and TI_{amb} = 8% in Fig. 14. It is observed that both field reconstruction techniques lead to high coherence in proximity of the principal load frequencies, such as the rotational (1P for blade, and 3P for the tower, see Fig. A1 for more details), the natural frequency of the tower ($\approx$ 0.25 Hz, which is close to the 3P at 6 m/s), and the dominant wake meandering frequency ($\approx$ 0.016 Hz). In general, the coherence from the CS simulations is non-zero at frequency up to 0.7 Hz (6P), and is higher compared to that from WDS simulations. This confirms that higher frequency fluctuations can be reconstructed more accurately using the CS approach.

By increasing the spatial and temporal resolutions of the scanning pattern, and neglecting volume-averaging effects, the CS-approach could potentially reconstruct the whole spectrum of the loads. This presents a limitation of the WDS-approach, which only reconstructs turbulence structures corresponding to the size of the wake deficit. Finally, given the limitation of the reconstruction techniques to recover small-scale turbulence structures, as discussed in Fig. 6, the accuracy of tower loads, which are driven by high-frequency fluctuations (see Fig. A1), drops compared to that of the blades. This can partly explain the larger deviations of Δ_R, X_R and ρ, inherent of $\mathrm{MxTB_{DEL}}$ and relative to $\mathrm{MxBR_{DEL}}$, observed in Figs. 9, 11 and 13, as well as the evidence that Δ_R of the $\mathrm{MxTB_{DEL}}$ is the most improved when the probe volume size is neglected, as seen in Fig. 9.

4.3 Sensitivity analysis

The load validation of Sect. 4.2 is carried out using statistics collected under near-neutral conditions at Alpha Ventus, i.e., low atmospheric turbulence. Nevertheless, atmospheric turbulence conditions has a strong impact on the wake development (Kumer et al., 2017; Zhan et al., 2020), and wind turbine loads (Sathe et al., 2013; Kretschmer et al., 2018). Further, the lidar measuring

https://doi.org/10.5194/wes-2020-104
Preprint. Discussion started: 24 September 2020

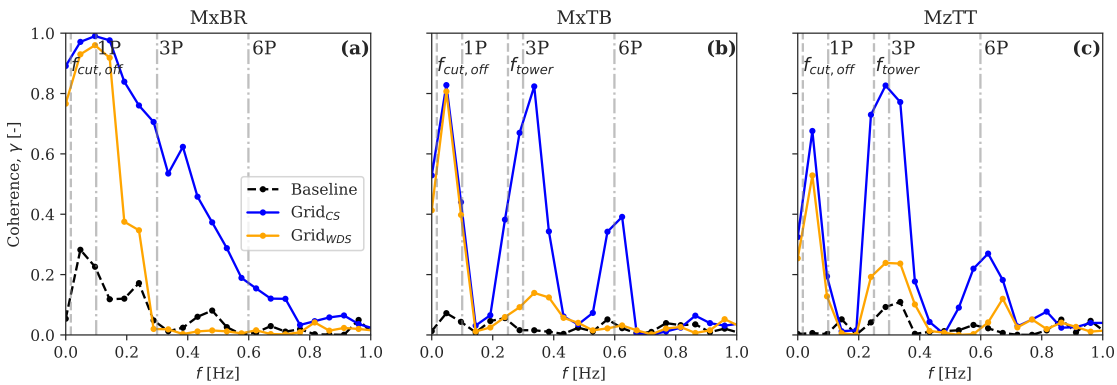

Figure 14. Spectral coherence analysis between the lidar-based load predictions and the $target$ simulations for **(a)** the blade root flapwise bending moment MxBR, **(b)** tower bottom fore-aft bending moment MxTB, and **(c)** yaw moment MzTT. The $target$ simulations are run for U_{amb} = 6 m/s and TI_{amb} = 8%. The $baseline$'s results are also shown in dashed black line, together with the principal operational frequencies of the wind turbine (1P ≈ 0.1 Hz, 3P and 6P) in dash-dot grey lines, the dominant frequency of the wake meandering $f_{cut,off}$ ≈ 0.016 Hz, and the natural frequency of the tower f_{tower} ≈ 0.25 Hz in dashed grey lines.

characteristics can impact the accuracy of reconstructed fields (Lundquist et al., 2015), thus that of load predictions. In the next subsections, we investigate the sensitivity of atmospheric turbulence conditions as well as selected lidar specifications on the accuracy of lidar-based load predictions using the Grid pattern as an example.

4.3.1 Effect of atmospheric turbulence conditions on load prediction accuracy

Figure 15a shows the sensitivity of the lidar-based load predictions bias for TI_{amb} within the range 4–20%. The high TI_{amb} leads to faster recovery of the velocity deficit (Doubrawa et al., 2019), amplifies the wake meandering (Machefaux et al., 2016), and affects the accuracy of lidar-reconstructed fields (Pettas et al., 2020) . This has a negligible effect on the accuracy of load predictions obtained with the CS-fields, while larger deviations are observed for the WDS results. This is partly due to the limited scanned area by the lidar combined with the large wake displacements. Indeed, the fitting procedure intrinsic of the WDS approach can lead to an inaccurate estimation of the wake shape parameters, when the wake moves out of the scanned area (Trujillo et al., 2011).

We investigate the influence of the atmospheric turbulence length scale on the load prediction accuracy in Fig. 15b, by varying L between 5 and 70 m. Earlier studies have shown the strong dependency of load statistics on the turbulence length scales (Sathe et al., 2013; Dimitrov et al., 2017; Conti et al., 2020). Further, L provides a measure of the resolution of the scanning configuration useful for performing constraints (Dimitrov and Natarajan, 2017). The turbulence length scale affects the predicted statistics of the explained variance ratio of the CS-fields, which decreases from $\rho_E^2 \sim$ 0.8 for $L = 29$ m to $\rho_E^2 \sim$ 0.6 for $L = 5$ m (not shown). This indicates that when L is low, the turbulence structure sizes fall below the sampling fidelity

https://doi.org/10.5194/wes-2020-104
Preprint. Discussion started: 24 September 2020

WIND ENERGY SCIENCE DISCUSSIONS
Open Access

of the CS approach (note that a spatial resolution of 29 m is assumed for the Grid as described in Sect. 3.3). The biases of the CS-based load predictions show a dependency on the turbulence length scales, while the WDS-fields are not significantly affected (see Fig. 15b).

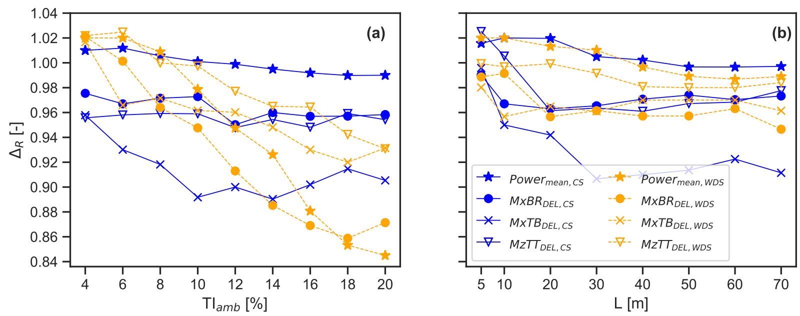

Figure 15. Influence of atmospheric turbulence conditions on the lidar-based load prediction accuracy, including: **(a)** the effect of ambient turbulence (T_{amb}) given U_{amb} = 6 m/s, **(b)** the effect of turbulence length scale, L, given U_{amb} = 6 m/s and TI_{amb} = 8%. The bias Δ_R at each nominal value is computed from 18 simulated seeds. The Grid pattern is used for the analysis.

4.3.2 Effect of lidar probe volume and scanning period on load prediction accuracy

One of the main limitations of CW lidars is that the probe volume size increases proportionally with the square of the focal distance (Sathe and Mann, 2013). As the diameter of modern wind turbines has reached 200 m, as for the DTU 10 MW, measuring at farther distances upfront of the rotor becomes an issue due to the larger probe volumes. Hence, we investigate the sensitivity of the lidar probe volume on the load prediction accuracy in Fig. 16a, by varying the probe volume length between 0 to 210 m. It is seen that the magnitude of Δ_R decreases almost linearly with increasing probe volume lengths. Further, the probe volume effects are more pronounced for the CS-approach, which directly incorporates the low-pass filtered wind speed fluctuations into the reconstructed field.

Another limitation inherent of the PL lidar technology is the reduced sampling frequency compared to CW lidars (Peña et al., 2015). The sensitivity of the lidar sampling frequency on the load prediction accuracy is assessed by varying the scanning period, which is defined as the time to complete a full scan (1–30 s). For this particular analysis, the $target$ simulations are run for U_{amb} = 6 m/s and TI_{amb} = 16%. Although the scanning period does not play an important contribution to the load prediction accuracy, as shown in Fig. 16-b, this outcome is conditional to the dominant frequency of the wake meandering, which in turn decreases with larger rotors ($f_{cut,out} = U_{amb}/(2D)$), and the spatial resolution of the pattern. The CS-results show that accurate power predictions are obtained up to a scanning period ≈20 s, which corresponds to one third of the wake meandering dominant period.

https://doi.org/10.5194/wes-2020-104
Preprint. Discussion started: 24 September 2020

WIND ENERGY SCIENCE DISCUSSIONS

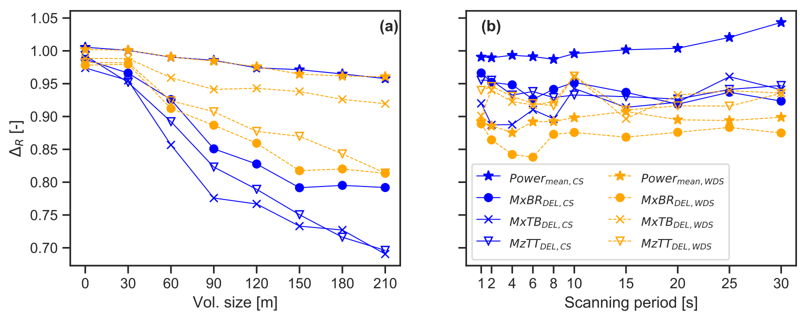

Figure 16. Influence of lidar scanning specifications on the lidar-based load prediction accuracy, including: **(a)** the effect of probe volume size given U_{amb} = 6 m/s and TI_{amb} = 8%, **(b)** the effect of the scanning period given U_{amb} = 6 m/s and TI_{amb} = 16%. The bias Δ_R at each nominal value is computed from 18 simulated seeds. The Grid pattern is used for the analysis.

5 Discussion

This study addresses the need for reducing the statistical load prediction uncertainty of wind turbines operating in wake conditions by incorporating lidar measurements in the wake field reconstruction. One of the main elements used in the study is to consider as *target* the wake flow fields generated by the DWM model. The DWM model is a simplified engineering wake model subjected to modelling uncertainties. Although the wake deficit and turbulence fields can deviate from high-fidelity simulations, or field data, the calibration of the DWM model coefficients can considerably improve the accuracy and provide quasi-steady wake characteristics in good agreement with observations (Reinwardt et al., 2020) and simulations (Keck et al., 2012, 2014, 2015). This modelling uncertainty is not expected to significantly alter the findings of this study, as we demonstrate the robustness of the lidar-based approaches under a large variety of inflow wind and operational conditions. Further, wake-added turbulence spectral properties are described, to the extent needed for the load analysis, by an isotropic Mann-generated turbulence field with low length scale (Madsen et al., 2005). A more realistic modelling choice to accurately simulate the turbulence structures within the wake fields is found in large-eddy simulations (LES). In comparison to DWM simulated fields, the LES fields can potentially influence the load predictions (Churchfield et al., 2015; Nebenführ and Davidson, 2017), and the accuracy of reconstructed fields (Bauweraerts and Meyers, 2020). Note that the computational burden of high-fidelity simulations, such as LES, would make the statistical load analysis unfeasible.

Another limitation stems from the lidar simulator used in the study, which replaces full-field lidar measurements. Real lidar data taken upfront the rotor should be corrected for induction (Borraccino et al., 2017; Mann et al., 2018), blade blockage effects, and wind evolution (Bossanyi, 2013; de Mare and Mann, 2016). These effects are not simulated due to the modeling assumptions of the DWM model. In spite of the aforementioned limitations, this numerical framework allows us to assess the influence of several uncertainty sources and to evaluate different lidar scanning strategies under a variety of inflow wind conditions in an idealized yet fully controllable environment.

https://doi.org/10.5194/wes-2020-104
Preprint. Discussion started: 24 September 2020

The load analysis indicates that the field reconstruction techniques, lidar scanning strategies, and lidar's probe volume sizes have a significant influence on the accuracy of load assessment. Nevertheless, both the CS- and WDS-approaches can reconstruct to a large extent the wake dynamics that have the strongest impact on the power and load predictions. These include the spatial distribution of the velocity deficit and the added turbulence resulting from its motions in time. The lidar-based predicted load statistics are comparable to the results obtained with the IEC-recommended DWM model ($\Delta_R \sim 0.97$ – 1.01). Furthermore, the statistical uncertainty of the lidar-based load predictions is considerably reduced by a factor between 1.2–5 compared to DWM's results (the $baseline$). By combining lidar measurements with the CS- and WDS-reconstruction approaches, we are able to simulate power and load time-series with strong similarities to the actual measured turbine responses, as shown in Sect. 4.2.4.

Yet, the characterization of the small scale turbulence poses a challenge given the current limitations of lidar's sampling frequency and probe volume size (Peña et al., 2017). The small scale wake-added turbulence enhances the energy spectral content in the high-frequency range, 1–20 Hz (Madsen et al., 2010; Chamorro et al., 2012; Singh et al., 2014), and its contribution on the fatigue damage varies according to the load component and turbine operational strategy (Tibaldi et al., 2015). Bergami and Gaunaa (2014) demonstrates that the strongest fatigue damage on the blades occurs at frequencies around 1P (0.1–0.16 Hz for the DTU 10 MW), whereas structures as tower top (nacelle) and tower bottom are mainly affected by the tower eigenfrequency (0.25 Hz) and the 3P frequency (0.3–0.48 Hz). As the PSD of tower loads exhibits large energy spectral content at high frequencies (see Fig. A1), the accuracy of tower load predictions decreases compared to that achieved by blade loads, as seen in Sects. 4.2.4 and 4.2.5.

We demonstrate that a high spatial resolution of the lidar scanning pattern is required to ensure an acceptable level of accuracy. Our results reveal that the current commercially available nacelle-mounted lidars, here represented by the 4P, 7P and Cone patterns, will not provide sufficient information to accurately reconstruct the wake fields for the purpose of the load validation in wakes. The scanning requirements are met by the SL, and any arbitrary lidar that can potentially scan a greater region of the rotor, as for the here-simulated Grid configuration. Although we do not optimize the scanning strategies, it is inferred that the required spatial resolution depends on the size of the wake turbulence structures in the wind field.

It is observed that incorporating a sufficient number of lidar measurements directly in the turbulence field can produce more accurate load predictions, compared to assuming a generic functional shape of the wake deficit. This is shown by the time-series analysis in Sect. 4.2.4 and the spectral coherence analysis of Sect. 4.2.5, which illustrate that high frequency load fluctuations can be reconstructed more accurately by the CS- than the WDS-approach. Furthermore, the constrained field technique based on the Mann turbulence model can be extended to incorporate the v- and w-turbulence fluctuations, as demonstrated in Dimitrov and Natarajan (2017). Additionally, the CS-method finds direct application for reconstructing more complex flow fields occurring in wind farms, e.g., multiple wakes.

The accuracy of the WDS-predicted loads is conditional to the goodness of the selected shape function to represent velocity deficits. The wake deficit can deviate from a Gaussian pattern as the atmosphere becomes more unstable (Ning and Wan, 2019), whereas it exhibits a double-peak shape in the near-wake region (Keck et al., 2014), and a more complex geometry in a multiple wake scenario. Our results show that combining a physical-based wake deficit formulation with actual lidar measurements of

https://doi.org/10.5194/wes-2020-104
Preprint. Discussion started: 24 September 2020

the wake meandering path can potentially reduce the statistical uncertainty of load predictions. Overall, the fitting procedure of the WDS-approach is relatively fast and can provide reliable real-time wake field estimates not only for load validation purposes, but also for improving wind farm monitoring and control strategies. On the other hand, the computational expenses of the CS-approach increase considerably with the amount of constraints simulated and the dimension of the turbulence boxes. For reference, a single wind field with 27900 constraints (i.e. SL) and a turbulence box with a grid size of 8192×32×32 points currently requires one and a half hour of simulation time on a single CPU.

6 Conclusions

This study proposed two alternative wind turbine load validation procedures under wake conditions that reconstruct synthetic wake fields from time series of lidar retrievals. The first approach consisted in incorporating lidar data of the wake field directly into random Mann turbulence field realizations. The second approach relied on the superposition of lidar-fitted bivariate Gaussian wake deficit time-series into the Mann turbulence fields.

We developed a numerical framework that uses a virtual lidar simulator to scan synthetic wake flow fields simulated by the DWM model, which were referred to as the actual $target$ fields. The virtual lidar data were provided as input to the field reconstruction approaches. Thus, we carried out aeroelastic simulations with the lidar-reconstructed wake fields and quantified the load predictions uncertainty against results obtained with the $target$.

It was found that lidar-reconstructed fields can potentially recover the main wake characteristics influencing power and load predictions, such as the spatial distribution of the velocity deficit and its dynamics within the simulated fields. This led to mean power and fatigue load estimates comparable with predictions of the DWM model ($\Delta_R \sim 0.97 - 1.01$), and a significant reduction of the statistical uncertainty (realization-to-realization) by a factor 1.2–5. The reduced statistical uncertainty was explained by improved predictions of power and load time-series, which showed a high degree of correlation with the $target$ turbine responses ($\rho \sim$ 0.33–0.99).

It was also demonstrated that the accuracy of the load predictions is mainly conditional on the spatial resolution of the lidar's scanning pattern, the size of the probe volume, and the adopted field reconstruction technique. Further investigations should validate the here-proposed approaches with full-field data collected in operating wind farms.

https://doi.org/10.5194/wes-2020-104
Preprint. Discussion started: 24 September 2020

Open Access
WIND ENERGY SCIENCE DISCUSSIONS

Appendix A: Power Spectral Density (PSD) of load predictions

Figure A1 shows a comparison of the PSD of MxBR, MxTB, and MzTT between the lidar-reconstructed and $target$ simulations run at U_{amb} = 6 m/s and TI_{amb} = 8%. Figure A1a displays the PSD of MxBR, where the first three peaks correspond to the subsequent rotor harmonics (1P, 2P and 3P). The highest observed peak is at 1P ($\sim$ 0.1 Hz), which indicates that the greatest load cycle amplitude is due to asymmetric blade loading condition. This effect is amplified by the in-homogeneous wake field approaching the rotor. Compared to the rotating blades, the PSD of the tower loads MxTB and MzTT exhibits the largest energy content at higher frequencies (> 3P $\sim$ 0.3 Hz). Further, the natural frequency of the tower (0.25 Hz) corresponds nearly to the 3P frequency at 6 m/s. This explains the very high peak seen for the MxTB. Overall, the PSD produced by the simulations with lidar-reconstructed fields (CS and WDS) shows good agreement with that of the $target$ simulations, meaning that the energy content is not being shifted between frequencies. However, it is observed that the energy content at high frequency (>1 Hz), induced by the wake-added turbulence, is not fully recovered due to the lidar probe volume and limited sampling frequency.

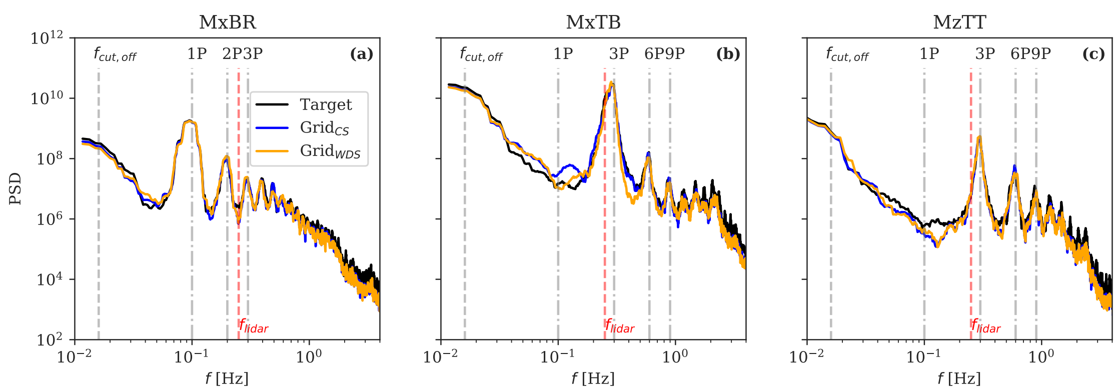

Figure A1. Power spectral density (PSD) of **(a)** the blade root flapwise bending moment MxBR, **(b)** tower bottom fore-aft bending moment MxTB, and **(c)** yaw moment MzTT. The dominant frequency of the wake meandering $f_{cut,off}$ = 0.016 Hz, the Nyquist frequency of the lidar f_{lidar} = 0.25 Hz (corresponding to the scanning period), and the main rotational frequencies 1P, 2P, 3P, 6P and 9P are shown. The $target$ simulations are run at 6 m/s with TI_{amb} = 8%.

https://doi.org/10.5194/wes-2020-104
Preprint. Discussion started: 24 September 2020

WIND ENERGY SCIENCE DISCUSSIONS

Acknowledgements. The work conducted by Vasilis Pettas is funded by the German Federal Ministry for Economic Affairs and Energy (BMWi) in the framework of the national joint research project RAVE - OWP Control (ref, 0324131B).

https://doi.org/10.5194/wes-2020-104
Preprint. Discussion started: 24 September 2020

References

International Standard IEC61400-13: Wind turbines - Part 13: Measurement of mechanical loads, Standard, IEC, 2015.

International Standard IEC61400-12-1: Wind energy generation systems - Part 12-1: Power performance measurements of electricity producing wind turbines, Standard, IEC, 2017.

International Standard IEC61400-1: wind turbines—part 1: design guidelines, Fourth; 2019, Standard, IEC, 2019.

Ainslie, J.: Calculating the flow field in the wake of wind turbines, Journal of Wind Engineering and Industrial Aerodynamics, 27, 213–224, https://doi.org/10.1016/0167-6105(88)90037-2, 1988.

Ainslie, J. F.: WAKE MODELLING AND THE PREDICTION OF TURBULENCE PROPERTIES, Proceedings of the Bwea Wind Energy Conference (british Wind Energy Association), pp. 115–120, 1986.

Bak, C., Zahle, F., Bitsche, R., Teaseong, K., Yde, A., LC, H., Natarajano, A., and Hansen, M.: Description of the DTU 10MW reference wind turbine, 2013.

Barthelmie, R. J., Hansen, K. S., Frandsen, S. T., Rathmann, O., Schepers, J., Schlez, W., Phillips, J., Rados, K., Zervos, A., Politis, E., and Chaviaropoulos, P.: Modelling and Measuring Flow and Wind Turbine Wakes in Large Wind Farms Offshore, Wind Energy, 12, 431–444, https://doi.org/10.1002/we.348, 2009.

Bauweraerts, P. and Meyers, J.: Reconstruction of turbulent flow fields from lidar measurements based on large-eddy simulation, 2020.

Bergami, L. and Gaunaa, M.: Analysis of aeroelastic loads and their contributions to fatigue damage, Journal of Physics: Conference Series (online), 555, 012 007, https://doi.org/10.1088/1742-6596/555/1/012007, 2014.

Bingöl, F., Mann, J., and Larsen, G. C.: Light detection and ranging measurements of wake dynamics Part I: One-dimensional Scanning, Wind Energy, 13, 51–61, https://doi.org/10.1002/we.352, 2010.

Borraccino, A., Schlipf, D., Haizmann, F., and Wagner, R.: Wind Field Reconstruction from Nacelle-Mounted Lidars Short Range Measurements, Wind Energy Science, 2, 269–283, https://doi.org/10.5194/wes-2017-10, 2017.

Bos, R., Giyanani, A., and Bierbooms, W.: Assessing the severity ofwind gusts with lidar, Remote Sensing, 8, 758, https://doi.org/10.3390/rs8090758, 2016.

Bossanyi, E.: Un-freezing the turbulence: application to LiDAR-assisted wind turbine control, Iet Renewable Power Generation, 7, 321–329, https://doi.org/10.1049/iet-rpg.2012.0260, 2013.

Chamorro, L. P., Guala, M., Arndt, R. E., and Sotiropoulos, F.: On the evolution of turbulent scales in the wake of a wind turbine model, Journal of Turbulence, 13, 1–13, https://doi.org/10.1080/14685248.2012.697169, 2012.

Churchfield, M. J., Moriarty, P. J., Hao, Y., Lackner, M. A., Barthelmie, R., Lundquist, J. K., and Oxley, G. S.: A comparison of the dynamic wake meandering model, large-eddy simulation, and field data at the egmond aan Zee offshore wind plant, 33rd Wind Energy Symposium, pp. 20 pp., 20 pp., 2015.

Conti, D., Dimitrov, N., and Peña, A.: Aero-elastic load validation in wake conditions using nacelle-mounted lidar measurements, Wind Energy Science Discussions, 2020, 1–31, https://doi.org/10.5194/wes-2020-8, https://www.wind-energ-sci-discuss.net/wes-2020-8/, 2020.

de Mare, M. T. and Mann, J.: On the Space-Time Structure of Sheared Turbulence, Boundary-layer Meteorology, 160, 453–474, https://doi.org/10.1007/s10546-016-0143-z, 2016.

Dimitrov, N., Borraccino, A., Peña, A., Natarajan, A., and Mann, J.: Wind turbine load validation using lidar-based wind retrievals, Wind Energy, 22, 1512–1533, https://doi.org/10.1002/we.2385, 2019.

https://doi.org/10.5194/wes-2020-104
Preprint. Discussion started: 24 September 2020

Open Access
WIND ENERGY SCIENCE
DISCUSSIONS

Dimitrov, N. K. and Natarajan, A.: Application of simulated lidar scanning patterns to constrained Gaussian turbulence fields for load validation, Wind Energy, 20, 79–95, https://doi.org/10.1002/we.1992, 2017.

Dimitrov, N. K., Natarajan, A., and Mann, J.: Effects of normal and extreme turbulence spectral parameters on wind turbine loads, Renewable Energy, 101, 1180–1193, https://doi.org/10.1016/j.renene.2016.10.001, 2017.

Dimitrov, N. K., Kelly, M. C., Vignaroli, A., and Berg, J.: From wind to loads: wind turbine site-specific load estimation with surrogate models trained on high-fidelity load databases, Wind Energy Science, 3, 767–790, https://doi.org/10.5194/wes-3-767-2018, 2018.

Doubrawa, P., Barthelmie, R. J., Wang, H., Pryor, S. C., and Churchfield, M. J.: Wind turbinewake characterization from temporally disjunct 3-D measurements, Remote Sensing, 8, 939, https://doi.org/10.3390/rs8110939, 2016.

Doubrawa, P., Barthelmie, R. J., Wang, H., and Churchfield, M. J.: A stochastic wind turbine wake model based on new metrics for wake characterization, Wind Energy, 20, 449–463, https://doi.org/10.1002/we.2015, 2017.

Doubrawa, P., Debnath, M., Moriarty, P. J., Branlard, E., Herges, T. G., Maniaci, D. C., and Naughton, B.: Benchmarks for Model Validation based on LiDAR Wake Measurements, Journal of Physics: Conference Series, 1256, 012 024, https://doi.org/10.1088/1742-6596/1256/1/012024, 2019.

Fuertes, F. C., Markfort, C. D., and Porteacute-Agel, F.: Wind Turbine Wake Characterization with Nacelle-Mounted Wind Lidars for Analytical Wake Model Validation, Remote Sensing, 10, 668 (18 pp.), 668 (18 pp.), https://doi.org/10.3390/rs10050668, 2018.

Held, D. P. and Mann, J.: Detection of wakes in the inflow of turbines using nacelle lidars, Wind Energy Science, 4, 407–420, https://doi.org/10.5194/wes-4-407-2019, 2019a.

Held, D. P. and Mann, J.: Lidar estimation of rotor-effective wind speed - An experimental comparison, Wind Energy Science, 4, 421–438, https://doi.org/10.5194/wes-4-421-2019, 2019b.

Herges, T. G. and Keyantuo, P.: Robust Lidar Data Processing and Quality Control Methods Developed for the SWiFT Wake Steering Experiment, Journal of Physics: Conference Series, 1256, 012 005, https://doi.org/10.1088/1742-6596/1256/1/012005, 2019.

Keck, R.-E., Veldkamp, D., Aagaard Madsen, H., and Larsen, G. C.: Implementation of a Mixing Length Turbulence Formulation Into the Dynamic Wake Meandering Model, Journal of Solar Energy Engineering, 134, 021 012, https://doi.org/10.1115/1.4006038, 2012.

Keck, R.-E., de Mare, M. T., Churchfield, M. J., Lee, S., Larsen, G. C., and Aagaard Madsen, H.: On atmospheric stability in the dynamic wake meandering model, Wind Energy, 17, 1689–1710, https://doi.org/10.1002/we.1662, 2014.

Keck, R. E., De Maré, M., Churchfield, M. J., Lee, S., Larsen, G., and Madsen, H. A.: Two improvements to the dynamic wake meandering model: Including the effects of atmospheric shear on wake turbulence and incorporating turbulence build-up in a row of wind turbines, Wind Energy, 18, 111–132, https://doi.org/10.1002/we.1686, 2015.

Kretschmer, M., Schwede, F., Faerron Guzmán, R., Lott, S., and Cheng, P. W.: Influence of atmospheric stability on the load spectra of wind turbines at alpha ventus, Journal of Physics: Conference Series, 1037, 052 009, https://doi.org/10.1088/1742-6596/1037/5/052009, 2018.

Kretschmer, M., Pettas, V., and Cheng, P. W.: Effects of wind farm down-regulation in the offshore wind farm Alpha ventus, Asme 2019 2nd International Offshore Wind Technical Conference, Iowtc 2019, https://doi.org/10.1115/IOWTC2019-7554, 2019.

Kristensen, L., Lenschow, D., Kirkegaard, P., and Courtney, M.: The Spectral Velocity Tensor for Homogeneous Boundary Layer Turbulence, Boundary-layer Meteorology, 47, 149–193, https://doi.org/10.1007/BF00122327, 1989.

Kumer, V. M., Reuder, J., and Eikill, R. O.: Characterization of turbulence in wind turbine wakes under different stability conditions from static Doppler LiDAR measurements, Remote Sensing, 9, 242, https://doi.org/10.3390/rs9030223, 2017.

Larsen, G. C., Madsen Aagaard, H., Bingöl, F., Mann, J., Ott, S., Sørensen, J., Okulov, V., Troldborg, N., Nielsen, N. M., Thomsen, K., Larsen, T. J., and Mikkelsen, R.: Dynamic wake meandering modeling, 2007.

https://doi.org/10.5194/wes-2020-104
Preprint. Discussion started: 24 September 2020

Larsen, G. C., Madsen Aagaard, H., Thomsen, K., and Larsen, T. J.: Wake meandering: A pragmatic approach, Wind Energy, 11, 377–395, https://doi.org/10.1002/we.267, 2008.

Larsen, T. J., Aagaard Madsen, H., Larsen, G. C., and Hansen, K. S.: Validation of the dynamic wake meander model for loads and power production in the Egmond aan Zee wind farm, Wind Energy, 16, 605–624, https://doi.org/10.1002/we.1563, 2013.

Lee, S., Churchfield, M., Moriarty, P., Jonkman, J., and Michalakes, J.: Atmospheric and wake turbulence impacts on wind turbine fatigue loadings, 50th Aiaa Aerospace Sciences Meeting Including the New Horizons Forum and Aerospace Exposition, pp. AIAA 2012–0540, https://doi.org/10.2514/6.2012-540, 2012.

Lundquist, J. K., Churchfield, M. J., Lee, S., and Clifton, A.: Quantifying error of lidar and sodar doppler beam swinging measurements of wind turbine wakes using computational fluid dynamics, Atmospheric Measurement Techniques, 8, 907–920, https://doi.org/10.5194/amt-8-907-2015, 2015.

Machefaux, E., Larsen, G. C., Koblitz, T., Troldborg, N., Kelly, M. C., Chougule, A. S., Hansen, K. S., and Rodrigo, J. S.: An experimental and numerical study of the atmospheric stability impact on wind turbine wakes, Wind Energy, 19, 1785–1805, https://doi.org/10.1002/we.1950, 2016.

Madsen, Helge Aagaard, H., Larsen, G. C., and Thomsen, K.: Wake flow characteristics in low ambient turbulence conditions, Proceedings (cd-rom), 2005.

Madsen, H. A., Larsen, G. C., Larsen, T. J., Troldborg, N., and Mikkelsen, R. F.: Calibration and Validation of the Dynamic Wake Meandering Model for Implementation in an Aeroelastic Code, Journal of Solar Energy Engineering, 132, 041 014, https://doi.org/10.1115/1.4002555, 2010.

Mann, J.: The spatial structure of neutral atmospheric surface-layer turbulence, Journal of Fluid Mechanics, 273, 141–168, 1994.

Mann, J., Pena Diaz, A., Troldborg, N., and Andersen, S. J.: How does turbulence change approaching a rotor?, Wind Energy Science, 3, 293–300, https://doi.org/10.5194/wes-3-293-2018, 2018.

Medley, J., Barker, W., Harris, M., Pitter, M., Slinger, C., Mikkelsen, T., and Sjöholm, M.: Evaluation of wind flow with a nacelle-mounted, continuous wave wind lidar, Proceedings of Ewea 2014, 2014.

Moens, M., Coudou, N., and Philippe, C.: A numerical study of correlations between wake meandering and loads within a wind farm, Journal of Physics: Conference Series, 1256, 012 012, https://doi.org/10.1088/1742-6596/1256/1/012012, 2019.

Muller, Y. A., Aubrun, S., and Masson, C.: Determination of real-time predictors of the wind turbine wake meandering, Experiments in Fluids, 56, 1–11, https://doi.org/10.1007/s00348-015-1923-9, 2015.

Nebenführ, B. and Davidson, L.: Prediction of wind-turbine fatigue loads in forest regions based on turbulent LES inflow fields, Wind Energy, 20, 1003–1015, https://doi.org/10.1002/we.2076, 2017.

Ning, X. and Wan, D.: LES study of wake meandering in different atmospheric stabilities and its effects on wind turbine aerodynamics, Sustainability (switzerland), 11, 6939, https://doi.org/10.3390/su11246939, 2019.

Pedersen, M. M., Larsen, T. J., Madsen, H. A., and Larsen, G. C.: More accurate aeroelastic wind-turbine load simulations using detailed inflow information, Wind Energy Science, 4, 303–323, https://doi.org/10.5194/wes-4-303-2019, 2019.

Pettas, V., García, F. C., Kretschmer, M., Rinker, J. M., Clifton, A., and Cheng, P. W.: A numerical framework for constraining synthetic wind fields with lidar measurements for improved load simulations, https://doi.org/10.2514/6.2020-0993, https://arc.aiaa.org/doi/abs/10.2514/6.2020-0993, 2020.

https://doi.org/10.5194/wes-2020-104
Preprint. Discussion started: 24 September 2020

WIND ENERGY SCIENCE DISCUSSIONS

Peña, A., Hasager, C. B., Badger, M., Barthelmie, R. J., Bingöl, F., Cariou, J.-P., Emeis, S., Frandsen, S. T., Harris, M., Karagali, I., Larsen, S. E., Mann, J., Mikkelsen, T., Pitter, M., Pryor, S., Sathe, A., Schlipf, D., Slinger, C., and Wagner, R.: Remote Sensing for Wind Energy, 2015.

Peña, A., Mann, J., and Dimitrov, N. K.: Turbulence characterization from a forward-looking nacelle lidar, Wind Energy Science, 2, 133–152, https://doi.org/10.5194/wes-2-133-2017, 2017.

Peña, A., Mann, J., and Rolighed Thorsen, G.: SpinnerLidar measurements for the CCAV52, 2019.

Reinwardt, I., Schilling, L., Dalhoff, P., Steudel, D., and Breuer, M.: Dynamic wake meandering model calibration using nacelle-mounted lidar systems, Wind Energy Science, 5, 775–792, https://doi.org/10.5194/wes-5-775-2020, 2020.

Rettenmeier, A., Schlipf, D., Würth, I., and Cheng, P. W.: Power performance measurements of the NREL CART-2 wind turbine using a nacelle-based lidar scanner, Journal of Atmospheric and Oceanic Technology, 31, 2029–2034, https://doi.org/10.1175/JTECH-D-13-00154.1, 2014.

Sathe, A. and Mann, J.: A review of turbulence measurements using ground-based wind lidars, Atmospheric Measurement Techniques, 6, 3147–3167, https://doi.org/10.5194/amt-6-3147-2013, 2013.

Sathe, A., Mann, J., Barlas, T. K., Bierbooms, W., and van Bussel, G.: Influence of atmospheric stability on wind turbine loads, Wind Energy, 16, 1013–1032, https://doi.org/10.1002/we.1528, 2013.

Schlipf, D., Schlipf, D. J., and Kuehn, M.: Nonlinear model predictive control of wind turbines using LIDAR, Wind Energy, 16, 1107–1129, https://doi.org/10.1002/we.1533, 2013.

Simley, E., Pao, L. Y., Kelley, N., Jonkman, B., and Frehlich, R.: LIDAR wind speed measurements of evolving wind fields, 50th Aiaa Aerospace Sciences Meeting Including the New Horizons Forum and Aerospace Exposition, pp. AIAA 2012–0656, https://doi.org/10.2514/6.2012-656, 2012.

Simley, E., Y. Pao, L., Frehlich, R., Jonkman, B., and Kelley, N.: Analysis of Wind Speed Measurements using Continuous Wave LIDAR for Wind Turbine Control *†, 2013.

Simley, E., Fürst, H., Haizmann, F., and Schlipf, D.: Optimizing lidars for wind turbine control applications-Results from the IEA Wind Task 32 workshop, Remote Sensing, 10, 863, https://doi.org/10.3390/rs10060863, 2018.

Singh, A., Howard, K. B., and Guala, M.: On the homogenization of turbulent flow structures in the wake of a model wind turbine, Physics of Fluids, 26, 025 103, https://doi.org/10.1063/1.4863983, 2014.

Tibaldi, C., Henriksen, L. C., Hansen, M. H., and Bak, C.: Wind turbine fatigue damage evaluation based on a linear model and a spectral method, Wind Energy, 19, 1289–1306, https://doi.org/10.1002/we.1898, 2015.

Trujillo, J.-J., Bingöl, F., Larsen, G. C., Mann, J., and Kühn, M.: Light detection and ranging measurements of wake dynamics. Part II: two-dimensional scanning, Wind Energy, 14, 61–75, https://doi.org/10.1002/we.402, 2011.

Wagner, R., Friis Pedersen, T., Courtney, M., Antoniou, I., Davoust, S., and Rivera, R.: Power curve measurement with a nacelle mounted lidar, Wind Energy, 17, 1441–1453, https://doi.org/10.1002/we.1643, 2014.

Zhan, L., Letizia, S., and Valerio Iungo, G.: LiDAR measurements for an onshore wind farm: Wake variability for different incoming wind speeds and atmospheric stability regimes, Wind Energy, 23, 501–527, https://doi.org/10.1002/we.2430, 2020.

Zwick, D. and Muskulus, M.: The simulation error caused by input loading variability in offshore wind turbine structural analysis, Wind Energy, 18, 1421–1432, https://doi.org/10.1002/we.1767, 2015.